

COMPUTATION OF FLOW THROUGH BENDS

by

J A Sattary, M J Reader-Harris and L A Johnstone

NEL, East Kilbride, Glasgow

SUMMARY

Computations have been performed for flow through a single 90° swept bend and through two 90° swept bends, both in the same plane (S-configuration) and in perpendicular planes. Further computations were carried out in which the two bends were separated by a distance of 9D. The computational results show very good agreement with experimental data and give confidence in the ability of CFD to model flow in pipe bends accurately. Hence, a better understanding of the behaviour of flow downstream of bend installations has been obtained. The work reported in this paper shows that good installation design can eliminate some of the more severe flow conditions.

The S-bend with no separation between bends produces a very flat downstream velocity profile compared with those downstream of the single bend or the S-bend with 9D separation. The twisted S-bend with 9D separation between the bends does not produce swirl; this is confirmed by experimental data.

1 INTRODUCTION

This paper describes computational work undertaken by NEL within the Header Research Consortium project. The work has been supported by a Consortium consisting of Amerada Hess, Amoco, Daniel Industries, Gas Research Institute, Kvaerner H&G Offshore, N.V. Nederlandse Gasunie, Shell Expro and the UK Department of Trade and Industry. The overall aim of the project was to investigate the effectiveness of flow conditioners downstream of headers and bends, both as regards flow profiles and in terms of the performance of orifice meters; results of the experimental work were published in 1995¹.

Computational fluid dynamics (CFD) is a technique that is more frequently being used to predict flow profiles downstream of various pipe installations and their effect upon the performance of various types of flowmeter. The advantage of CFD over experimental measurements is that it gives profiles of all variables over the whole flow domain. This knowledge can be used to determine the effect of these profiles on various types of flowmeter.

Over the years many experimental measurements have been made of flow profiles downstream of various pipe installations, in particular downstream of single 90° swept bends and double bends. Hence, CFD results can be compared with experimental results to give confidence in the computational model. Profiles from any part of the domain can then

be used to obtain a better understanding of the behaviour of flow downstream of bend installations. This information is of importance to Standards. Also, good agreement between CFD and experiment in these configurations may make possible the use of CFD in the design of installations.

2 COMPUTATIONAL CODE

The commercially available CFD code FLUENT version 4.31² was run on a Silicon Graphics Indigo workstation. The standard k- ϵ turbulence model was used with the QUICK difference scheme. At the inlet a fully developed flow profile was specified with a mean velocity of 54 m/s and Reynolds number of approximately 8×10^5 . Details of the CFD code, boundary conditions and specifications are given in Appendix A.

3 GEOMETRY AND COMPUTATIONAL GRID

Each bend configuration was computed with a pipe diameter, D , of 0.254 m and a bend radius of $1.5D$.

A structured grid was used to divide the flow domain into cells. In order to increase the accuracy of the computed results it is necessary to maximise the number of cells used and to obtain an appropriate grid for a particular geometry. For comparison purposes the grids should be similar. Therefore, the grid in the axial direction is similar for all bend computations. Fig. 1 shows the node positions and bunching in the axial direction for the S-bend with $9D$ separation. It comprises: 14 cells for the $2D$ inlet, 20 cells on each bend, 40 cells for the $8D$ outlet pipe and 54 cells for the $9D$ of straight pipe between the bends. Two different cross-sectional grids were used in the computations; one for the S-bend and a different one for the twisted S-bend configurations; results were computed using both grids for the single 90° bend.

3.1 S-Bend (Fine Grid)

For the S-bend configurations the cross-sectional grid was 21×21 , as shown in Fig. 2. Since the geometry is symmetrical about the horizontal axis, it was only necessary to compute the flow in half of the pipe; thus this grid could be made fine in comparison with the twisted S-bend grid. With this type of grid a small hole is not computed in the centre of the pipe but it is assumed to have an insignificant effect on the results since its area is less than 0.01 per cent of the total cross-sectional area.

The bend geometries computed using this fine grid are: single 90° bend, S-bend with $0D$ separation and S-bend with $9D$ separation.

3.2 Twisted S-Bend (Coarse Grid)

For the twisted S-bend configurations computations were performed throughout the whole pipe using a cross-sectional grid of 21×21 (Fig. 3); thus this grid is much coarser than that for the S-bend configurations.

The bend geometries computed using this coarse grid are: single 90° bend, twisted S-bend with 0D separation and twisted S-bend with 9D separation.

4 COMPUTATIONAL RESULTS

The non-dimensional velocity magnitude, U , presented in this section is given by

$$U = \frac{(u^2 + v^2 + w^2)^{1/2}}{\bar{u}}$$

where u , v and w are the axial, tangential and radial velocity components respectively and \bar{u} is the mean axial velocity. Where transverse velocity vectors are presented the non-dimensional velocity magnitude, V , is the combination of the radial and tangential components only and is given by

$$V = \frac{(v^2 + w^2)^{1/2}}{\bar{u}}$$

4.1 Computational Results Using a Fine Grid

4.1.1 Single 90° bend

Fig. 4 shows a contour plot of the velocity magnitude for a slice on the horizontal plane (at the plane of symmetry). The maximum non-dimensional velocity magnitude, U_m , is 1.31 on the inside of the bend. The regions of minimum velocity are close to the outside of the bend and also near the inner wall less than 1D downstream of the bend.

(In the downstream straight pipe the region close to the pipe wall corresponding to the outer side of the nearest upstream bend is hereafter referred to as 'outer' and likewise the region corresponding to the inside of the nearest upstream bend is hereafter referred to as 'inner'. In the figures inner and outer are labelled as 'inside' and 'outside'.)

Fig. 5 shows contours of velocity magnitude for 8 cross-sectional slices downstream of the bend from 0D to 7D in approximately 1D increments. At 0D the maximum velocity has moved from the inside of the bend to close to the centreline. At 1D this maximum velocity has now been replaced by the minimum velocity and the maximum velocity is in the outer half of the pipe cross-section. At 3D and 4D this maximum velocity forms a crescent shape near the outer side of the slice. At 5D and 6D this maximum velocity decays and the crescent thins. At 7D the crescent has almost joined on the inner side of the slice and in the centre part of the slice the velocity profile is relatively flat and still less than the crescent velocity.

The velocity magnitude 4D downstream of the bend is shown in detail in Fig. 6. The maximum velocity is near the outer side of the slice where $U_m = 1.11$.

Fig. 7 shows transverse velocity vectors of the same slice 4D downstream of the bend. The shift of the maximum velocity from the inside of the bend to the outer side of the slice downstream causes flow along the axis of symmetry from the inner to the outer side of the

slice which in turn sets up two counter rotating vortices in the flow. The maximum non-dimensional velocity magnitude, V_m , is 0.22.

4.1.2 S-bend with no separation

Fig. 8 shows a contour plot of velocity magnitude for a slice at the plane of symmetry. As shown in Fig. 4, between 0D and 1D downstream of a single bend the velocity on the outer side of the bend is higher than that of a fully developed velocity profile. For the S-bend configuration with no separation between the bends this higher velocity enhances the velocity on the inner side of the second bend where $U_m = 1.44$. Conversely, the velocity on the outer side downstream of a single bend is lower than that of a fully developed flow profile and this acts to decrease the velocity even more on the outside of the bend.

Fig. 9 shows contours of velocity magnitude for 7 slices downstream of the second bend from 1D to 7D in approximately 1D increments. At 1D downstream of the second bend the crescent of maximum velocity is in the opposite direction to that observed downstream of the single 90° bend (Fig. 5); its back faces towards the inner side of the pipe where the minimum velocity is obtained. The profile 1D downstream is almost a mirror image of that at 4D downstream of the single bend (Fig. 6). Between 2D and 3D downstream the crescent disappears and at 4D the profile is very flat. Between 5D and 7D the area of minimum velocity on the outer side of the pipe appears to grow towards the centreline.

The velocity magnitude 4D downstream of the second bend is shown in detail in Fig. 10. It shows a very flat profile covering most of the pipe cross-section and $U_m = 1.03$.

Fig. 11 shows transverse velocity vectors of the same slice 4D downstream of the second bend. These are the combinations of the radial and tangential components of velocity. It is interesting to note that the velocity vectors along the axis of symmetry are in the opposite direction compared to those of the single bend (Fig. 7). Figs 7 and 11 are almost a mirror image of each other and $V_m = 0.16$, which is less than in the single bend case.

4.1.3 S-bend with 9D separation

Fig. 12 shows a contour plot of velocity magnitude for a slice at the plane of symmetry, for an S-bend with 9D separation between the bends. The velocity profile downstream of the first bend is the same as that downstream of the single bend. As with the S-bend with no separation the velocity magnitude on the inner side of the second bend is enhanced by the first bend. The maximum velocity is on the inner side of the second bend where $U_m = 1.39$, this is slightly lower than that of the S-bend with no separation.

Fig. 13 shows contours of velocity for 7 slices downstream of the second bend from 1D to 7D in approximately 1D increments. At 1D downstream of the second bend the crescent of maximum velocity is still in the opposite direction to that observed downstream of the single 90° bend (Fig. 5). The minimum velocity along the inner side is caused by the second bend and the lower velocity along the outer side is a result of the first bend. Between 2D and 6D downstream of the second bend this lower velocity along the outer side gradually decays. At 7D the crescent has spread and almost reversed.

The velocity magnitude 4D downstream of the second bend is shown in detail in Fig. 14. It shows a much flatter profile than that 4D downstream of the single bend (Fig. 6) but not as flat as 4D downstream of the S-bend with no separation (Fig. 10). On the inner side of the slice the minimum velocity covers a much larger area than it does downstream of the S-bend with no separation.

Fig. 15 shows transverse velocities of the same slice 4D downstream of the second bend. The velocity vectors along the axis of symmetry flow towards the centreline from both the inner side and outer side of the pipe wall. Instead of two there are four vortices of similar magnitude. The maximum velocity is towards the centre of the pipe where $V_m = 0.08$, half that for the S-bend with no separation at the same downstream distance.

4.2 Computational Results Using a Coarse Grid

4.2.1 Single 90° bend

The coarse grid shown in Fig 3 was also used to compute the single bend case to allow results for the two different grids to be compared for the same geometry. The results agree well and the velocity profiles look very similar to those with the fine grid (Figs 6 to 9).

4.2.2 Twisted S-bend with no separation

Fig. 16 shows a contour plot of velocity magnitude for a slice in the horizontal plane (the plane from the inner to the outer side of the pipe downstream of the second bend). The maximum velocity is on the inside of the second bend where $U_m = 1.35$ which is less than the value of U_m for the S-bend but more than that for the single bend.

Fig. 17 shows contours of velocity magnitude for 8 slices downstream of the second bend from 0D to 7D in approximately 1D increments. The profiles still retain the crescent shape but the region of minimum velocity progresses down the pipe in a clockwise direction (looking from bend to outlet).

The velocity magnitude at 4D downstream of the second bend is shown in detail in Fig. 18 and the corresponding transverse velocity vectors are shown in Fig. 19. Swirl dominates the profile and the position of the maximum velocity in Fig. 19 corresponds to the leading edge of the maximum velocity magnitude shown in Fig. 18.

4.2.3 Twisted S-bend with 9D separation

Fig. 20 shows a contour plot of velocity magnitude. The maximum velocity is in the same position as it is in the case of the twisted S-bend with no separation and of similar magnitude; $U_m = 1.34$.

Fig. 21 shows contours of velocity for 8 slices downstream of the second bend from 0D to 7D in approximately 1D increments. The area of minimum velocity along the length of the inner side and the area of maximum velocity along the outer side does not rotate as in the twisted S-bend with no separation case (Fig. 17). The profile does not change as rapidly from 1D to 7D as it does in the single bend case (Fig. 5).

The velocity magnitudes 4D downstream of the second bend are shown in detail in Fig. 22. Fig. 23 shows the combined radial and tangential components of the same slice 4D downstream of the second bend. This profile is not dominated by swirl; instead it has two counter-rotating vortices similar to the single bend case, although one vortex is more dominant and the profile is not symmetrical.

4.3 Comparison of Computational With Experimental Results

Figs 24 to 29 show comparisons of computational results using the fine grid given in Fig. 2 and the coarse grid given in Fig. 3, with experimental results in the plane of symmetry for the axial velocity at various distances downstream of the bend. The velocity profile data have been plotted non-dimensionally to allow comparison with experimental data. The inner wall is given by $r/R = -1$ and the outer wall is given by $r/R = +1$, where r is the radial distance from the pipe centreline and R is the pipe radius.

The $\frac{1}{8} D$ experimental data shown in Fig. 24 are LDV data for $D = 0.205\text{m}$ and $Re_D = 9 \times 10^5$ (Spearman³). The 4D experimental data shown in Fig. 25 are pitot traverse data obtained by NEL for the Header Research Consortium⁴: these data were obtained with $D = 0.254\text{ m}$ and $Re_D = 8 \times 10^5$. The 5D and 7D data shown in Figs 26 & 28 and in Figs 27 & 29 respectively are also LDV data obtained for $D = 0.1026\text{ m}$ and $Re_D \approx 5 \times 10^5$ (Spearman et al⁵).

Figs 24 to 27 show comparisons using both the fine and coarse grids for $\frac{1}{8} D$, 4D, 5D and 7D downstream of a single 90° bend. For the coarse grid, computations were performed using two different inlet profiles (for $n = 9.0$ and $n = 11.9$, where n is the exponent in the velocity profile power law equation, see Appendix A, equation A.7); in general the two different grids for $n = 9.0$ produced a much larger difference in the downstream velocity profiles than the difference in inlet profiles. The inlet velocity power law profile for $n = 9.0$ and the associated 5% limits specified in ISO 5167-1⁶ are also plotted for comparison.

The velocity profile for both the fine and coarse grid computations at $\frac{1}{8} D$ (Fig. 24) is much flatter than the experimental profile. For the fine grid the effect of the centreline hole is shown by the separation of the two points at $r/R = 0$. At 4D Fig. 25 shows very good agreement between experimental and computational data. At 5D Fig. 26 shows the experimental profile is now slightly flatter than the computational profile. Fig. 27 shows a marked decay in the peak of the experimental profile at 7D whereas the peak in the computational data, particularly using the fine grid, has only slightly decayed.

Figs 28 and 29 show comparisons using the coarse grid for 5D and 7D downstream of a twisted S-bend with no separation. It is more difficult to compare velocity profiles downstream of the twisted S-bend configuration because the profile across a single diameter changes more rapidly with downstream length owing to the corkscrew effect of the profile. At 5D (Fig. 28) the computational profile is flatter than the experimental profile and at 7D there is good agreement. For the same downstream length the profiles may agree better on a different diameter (ie for the comparison at 5D downstream (Fig 28) the computational profile on the diameter in the plane of symmetry agrees much better with

the profile of experimental data along the diameter of the perpendicular plane than it does with the experimental profile in the plane of symmetry).

For the twisted S-bend it is much better to compare the swirl angles with those of experimental data. The maximum swirl angle at 4D downstream of the twisted S-bend is 14.9° and is positioned near the wall at the position of the inside of the second bend (see Fig 19). The maximum swirl angle at 1D is 19.9° and is positioned near the wall halfway between the position of the inside of the first bend and the inside of the second bend. Mattingly and Yeh⁷ measured swirl angles for 1D, 5D and 11.7D downstream of a twisted S-bend and found swirl angles of 17° , 11° and 10° respectively; these data were means of two measurements taken at near wall positions on opposite sides of the pipe and are therefore expected to be slightly lower than the maximum. Mattingly and Yeh also measured swirl angles for a twisted S-bend with a 2.4D separation between the bends and found only 3.2° of swirl at 1D and 2.1° at 5D downstream of the second bend. For a twisted S-bend with a 5.3D separation they found only 2° of swirl at 1D and 1.3° at 5D downstream of the second bend. These experimental data confirm the findings for the computations of a twisted S-bend with 9D separation.

5 CONCLUSIONS

Computations have been performed for flow through a single 90° swept bend and through two 90° bends, both in the same plane (S-configuration) and in perpendicular planes. Further computations have been carried out in which the two bends are separated by a distance of 9D. For these configurations velocity profiles have been presented for a large part of the flow domain.

The computational results show good agreement with experimental data and give confidence in the ability of CFD to model flow in pipe bends accurately. Hence, a better understanding of the behaviour of flow downstream of bend installations has been obtained.

The S-bend with no separation between bends produces a very flat downstream velocity profile compared with those downstream of the single bend or the S-bend with 9D separation.

The twisted S-bend with 9D separation between the bends does not produce swirl; this is confirmed by experimental data.

Acknowledgements

This paper reports part of the work undertaken by NEL for the Header Research Consortium consisting of Amerada Hess, Amoco, Daniel Industries, Gas Research Institute, Kvaerner H&G Offshore, N.V. Nederlandse Gasunie, Shell Expro and the Department of Trade and Industry. The authors would like to thank the Header Research Consortium for their continued support and guidance.

This paper is published by permission of the Director and General Manager, NEL.

REFERENCES

- 1 READER-HARRIS, M. J., SATTARY, J. A. and WOODHEAD, E. The use of flow conditioners to improve flow measurement accuracy downstream of headers. Proceedings of the 3rd International Symposium on Fluid Flow Measurement. San Antonio, Texas, USA, March 1995.
- 2 FLUENT User's Guide. Version 4.3. January 1995. Fluent Europe Ltd., Holmwood House, Cortworth Rd, Sheffield, S11 9LP, UK.
- 3 SPEARMAN, E. P. Comprehensive LDV data on swirling and asymmetric flows through a conditioner/flowmeter package. NEL Report No 724. East Kilbride, Glasgow: National Engineering Laboratory, January 1992.
- 4 READER-HARRIS, M. J., WOODHEAD, E., SATTARY, J. A. and McEWEN, D. Flow conditions downstream of headers. HCP001 (223/94) Part 1. East Kilbride, Glasgow: National Engineering Laboratory, Sept 1995.
- 5 SPEARMAN, E. P., SATTARY, J. A., and READER-HARRIS, M. J. Comparison of velocity profiles downstream of perforated plate flow conditioners. Flomeko '94, Flow measurement in the mid-90s, 7th International conference on flow measurement, East Kilbride, Glasgow: National Engineering Laboratory, June 1994.
- 6 INTERNATIONAL ORGANIZATION FOR STANDARDIZATION. Measurement of fluid flow by means of orifice plates, nozzles and Venturi tubes inserted in circular cross-section conduits running full. ISO 5167-1, Geneva: International Organization for Standardization, 1991.
- 7 MATTINGLY, G. E., and YEH, T. T. Effects of pipe elbows and tube bundles on selected types of flowmeters. Flow Measurement and Instrumentation, Vol 2, pp 4-13, 1991.

APPENDIX A

NOTATION

C_1, C_2	Turbulence model coefficients	ϵ	Turbulence kinetic energy dissipation rate
C_μ	Turbulence model empirical constant	κ	von Karman's constant
E	Log law empirical constant	μ	Fluid viscosity
G_k	Generation term for k	μ_t	Turbulent viscosity
k	Turbulence kinetic energy	ρ	Fluid density
k_p	Turbulence kinetic energy at the near-wall grid point p	$\sigma_k, \sigma_\epsilon$	Turbulence model coefficients (Prandtl numbers)
n	Exponent in the velocity profile power law equation	τ	Wall shear stress.
R	Pipe radius		
Re_D	Reynolds number based on pipe diameter ($\rho \bar{u} D / \mu$)		
r	Radial distance from pipe centreline		
u	Local velocity		
u_{cl}	Centreline axial velocity		
u_p	Velocity at a point p near the wall		
u^+	Non-dimensional velocity = u/u^*		
u^*	Friction velocity = $(\tau/\rho)^{1/2}$		
\bar{u}	Mean velocity		
y_p	Distance from near-wall point p to the wall		
y^+	Non-dimensional distance from the pipe wall		

Details of the CFD code, the boundary conditions and specifications used for all computations are given below.

The k- ϵ turbulence model was used which has a turbulent viscosity given by

$$\mu_t = \rho C_\mu \frac{k^2}{\epsilon}, \quad (\text{A.1})$$

where $C_\mu = 0.09$, k is the turbulence kinetic energy, and ϵ is the turbulence kinetic energy dissipation rate. The differential transport equations for k and ϵ are:

$$\frac{\partial}{\partial t}(\rho k) + \frac{\partial}{\partial x_i}(\rho u_i k) = \frac{\partial}{\partial x_i} \left(\frac{\mu_t}{\sigma_k} \frac{\partial k}{\partial x_i} \right) + G_k - \rho \epsilon, \quad (\text{A.2})$$

$$\frac{\partial}{\partial t}(\rho \epsilon) + \frac{\partial}{\partial x_i}(\rho u_i \epsilon) = \frac{\partial}{\partial x_i} \left(\frac{\mu_t}{\sigma_\epsilon} \frac{\partial \epsilon}{\partial x_i} \right) + C_1 \frac{\epsilon}{k} G_k - C_2 \rho \frac{\epsilon^2}{k}, \quad (\text{A.3})$$

where G_k is the generation term for k and is given by the following formula:

$$G_k = \mu_t \left(\frac{\partial u_j}{\partial x_i} \right) \frac{\partial u_j}{\partial x_i}. \quad (\text{A.4})$$

The coefficients used are:

$$C_1 = 1.44, C_2 = 1.92, \sigma_k = 1.0 \text{ and } \sigma_\epsilon = 1.3.$$

The log-law of the wall can be used to compute the shear stress at the wall

$$\frac{u_p}{u^*} = u^+ = \frac{1}{\kappa} \ln(Ey^+) \quad (\text{A.5})$$

where u^* is the friction velocity, $(\tau/\rho)^{1/2}$, and

$$\kappa = 0.42 \text{ (von Karman's constant).}$$

Smooth pipewalls were assumed and for this case the roughness parameter, E , is 9.81.

The boundary conditions for k and ϵ are used to derive the following expression for y^+ , the non-dimensional distance from the pipe wall, given by

$$y^+ = \frac{\rho k_p^{1/2} C_\mu^{1/4} y_p}{\mu}, \quad (\text{A.6})$$

where y_p is the distance from the near-wall point p to the wall and k_p is the turbulence kinetic energy at that point.

At the inlet boundary a fully developed flow profile was specified using the following equations.

The axial velocity is represented by the empirical power law equation:

$$u = u_{cl}(1 - r/R)^{1/n} \quad (\text{A.7})$$

where $n = 9.0$ was used for the computations using the fine grid shown in Figs 4 to 15 and $n = 11.9$ for the computations using the coarse grid shown in Figs 16 to 23. In Figs 24 to 27 data computed with $n = 9.0$ and the coarse grid are also shown and the values of n are given for each set of computational data.

The turbulence kinetic energy is given by:

$$k = \frac{0.0121 + 0.0628 \left(\frac{r}{2R}\right)^{1.6}}{(2.95)^2} \bar{u}^2 \quad (\text{A.8})$$

and the turbulence kinetic energy dissipation rate is given by:

$$\varepsilon = \frac{9.277 \times 10^{-5}}{(R - r)} \bar{u}^3 \quad r/R > 0.686 \quad (\text{A.9})$$

$$\varepsilon = \frac{0.0026 + 0.274 \left(\frac{r}{2R}\right)^{2.9}}{51.34R} \bar{u}^3 \quad r/R \leq 0.686.$$

Equations (A.8) and (A.9) were derived from computations of flow in long straight pipes. The inlet radial velocity was zero and there was no swirl. At the outlet the default pressure boundary condition was specified. For the fine grid geometry a symmetry boundary was specified along the axis of symmetry and also for the centreline hole.

The QUICK (Quadratic Upstream Interpolation for Convection Kinematics) difference scheme was specified and the solution method used was SIMPLE (Semi-Implicit Method for Pressure-Linked Equations).

FLUENT was run until the normalised residuals were less than 10^{-4} .

The mean velocity, \bar{u} , was in each case set to 54.0 m/s giving $u_{cl} = 62.9$ m/s for $n = 9.0$ and $u_{cl} = 60.1$ m/s for $n = 11.9$. The density and viscosity were 1.1 kg/m^3 and $1.9 \times 10^{-5} \text{ kg m}^{-1} \text{ s}^{-1}$ respectively giving a Reynolds number, Re_D , of approximately 8×10^5 .

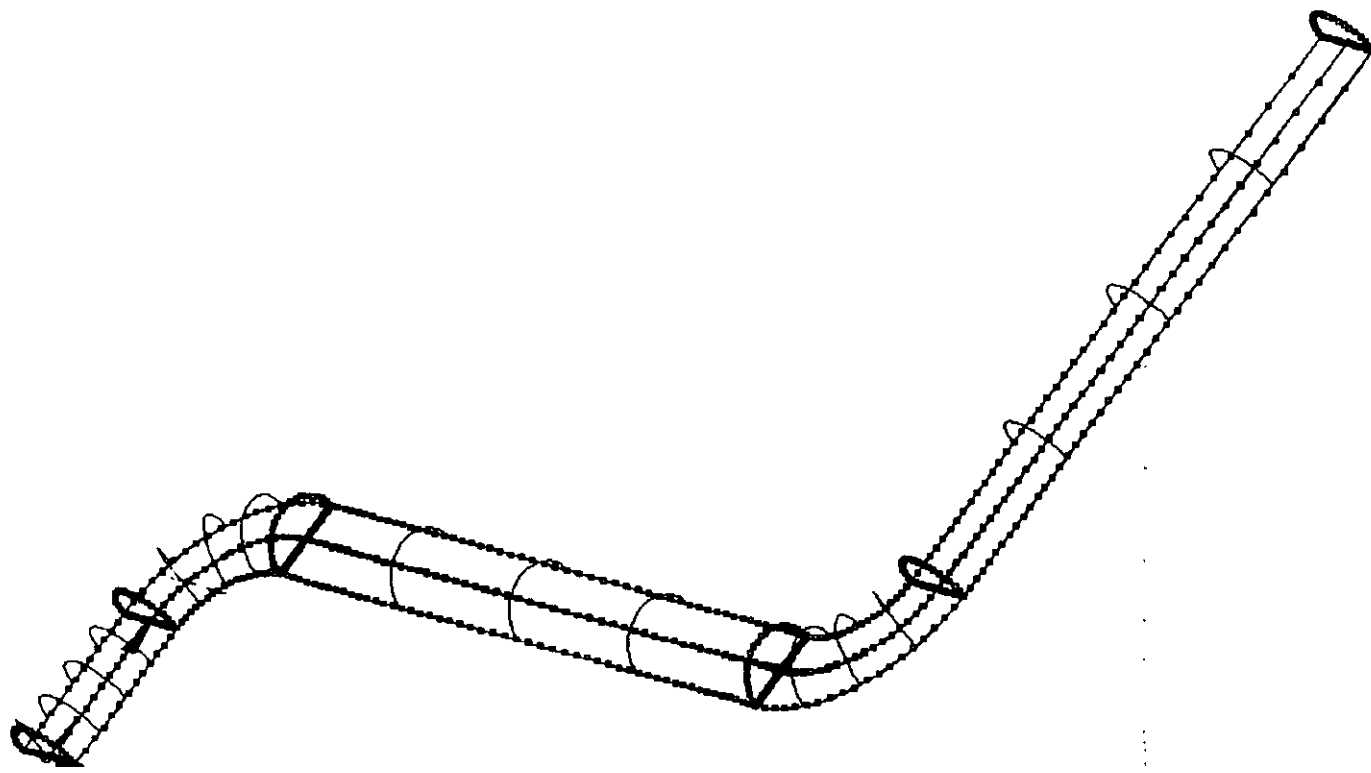


Fig. 1 Node Positions for the S-Bend with 9D Separation

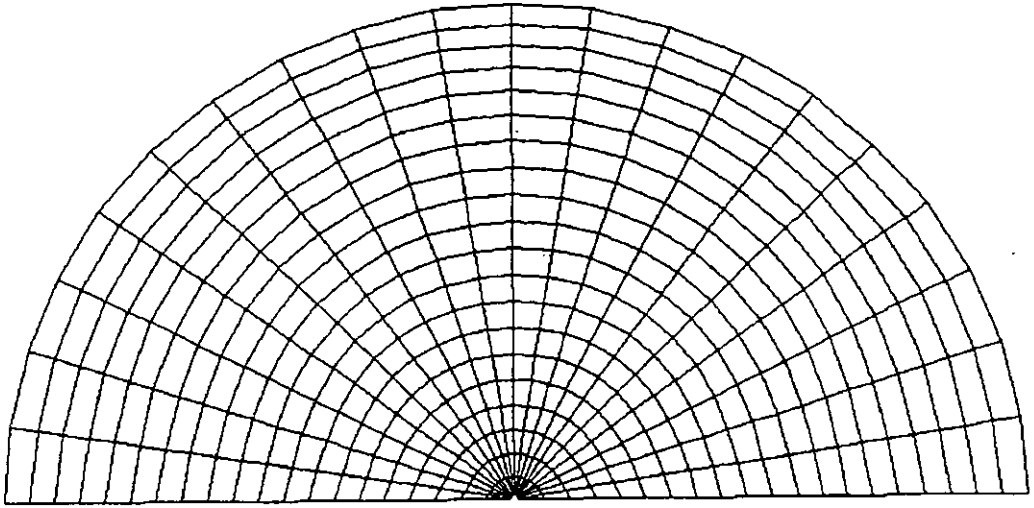


Fig. 2 S-Bend Cross-Sectional Grid (Fine Grid)

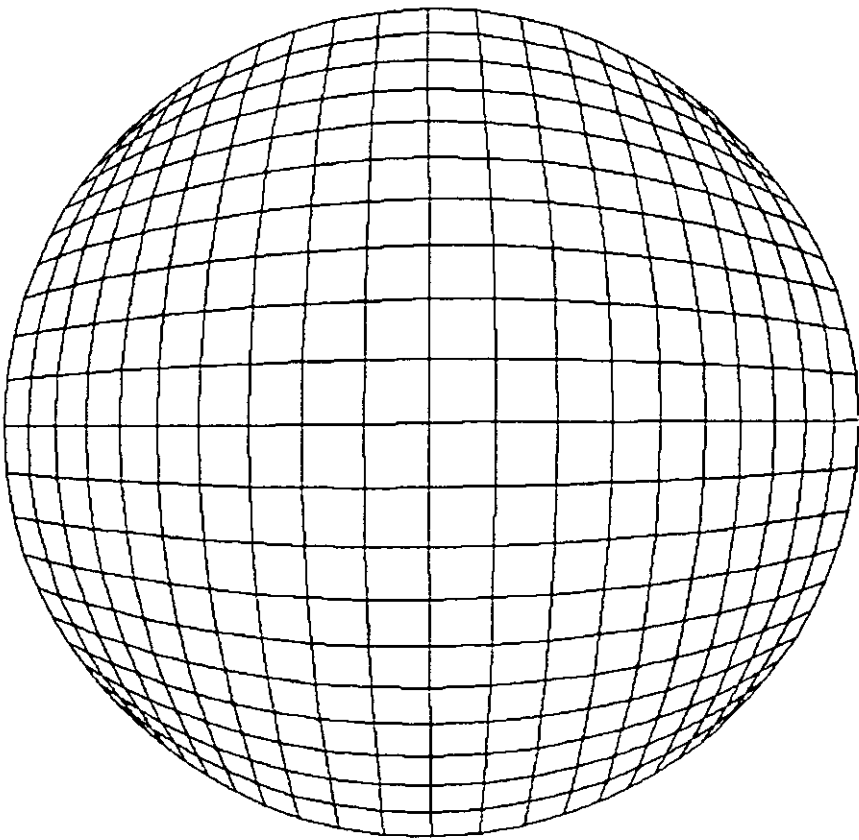
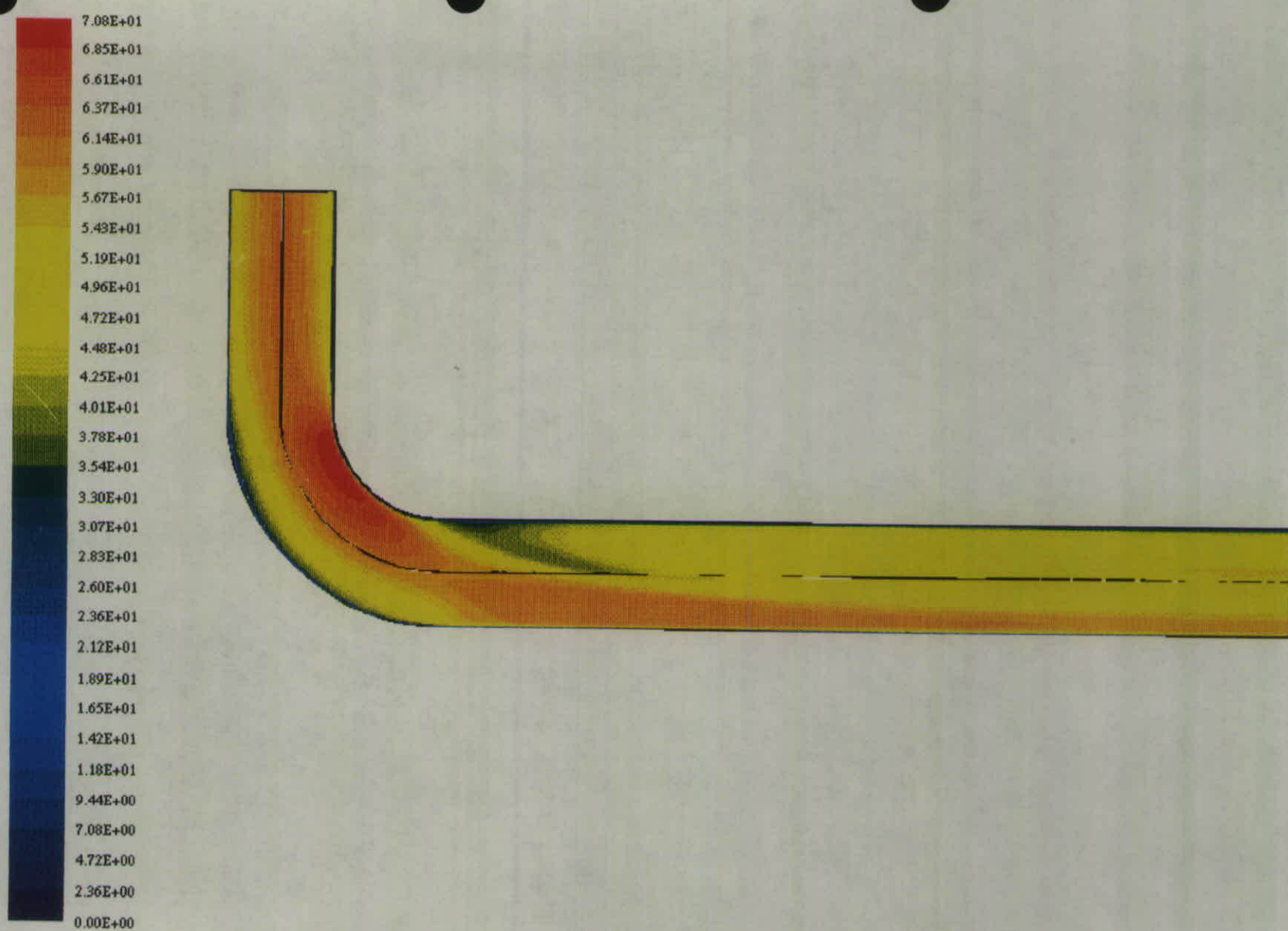


Fig. 3 Twisted S-Bend Cross-Sectional Grid (Coarse Grid)



NEL - Single 90 degree bend

Velocity Magnitude (M/S)

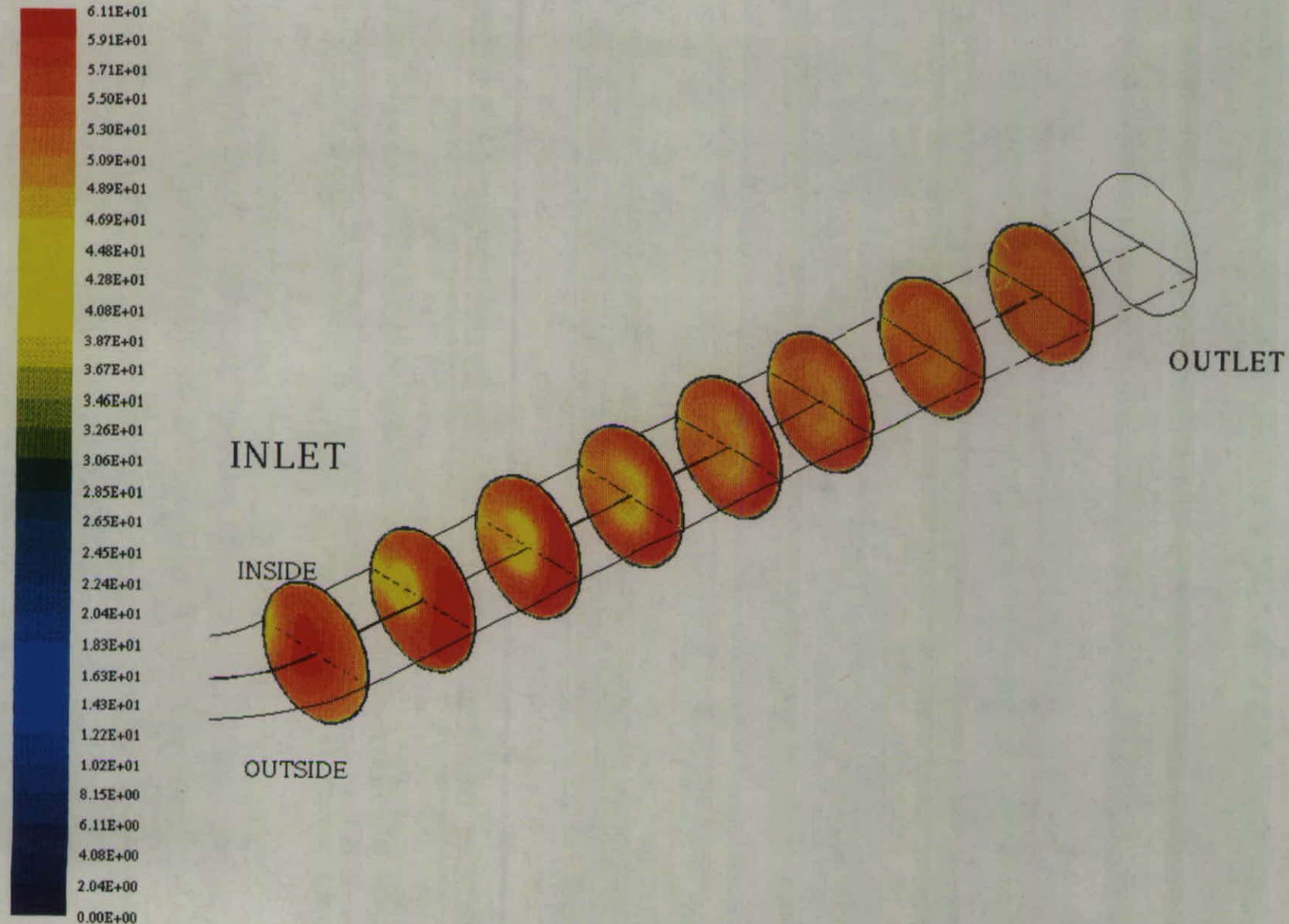
L max = 7.081E+01 L min = 0.000E+00



Fluent 4.31

Fluent Inc.

Fig. 4 Contours of Velocity Magnitude in the Plane of Symmetry for a Single Bend



NEL - Single 90 degree bend

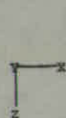
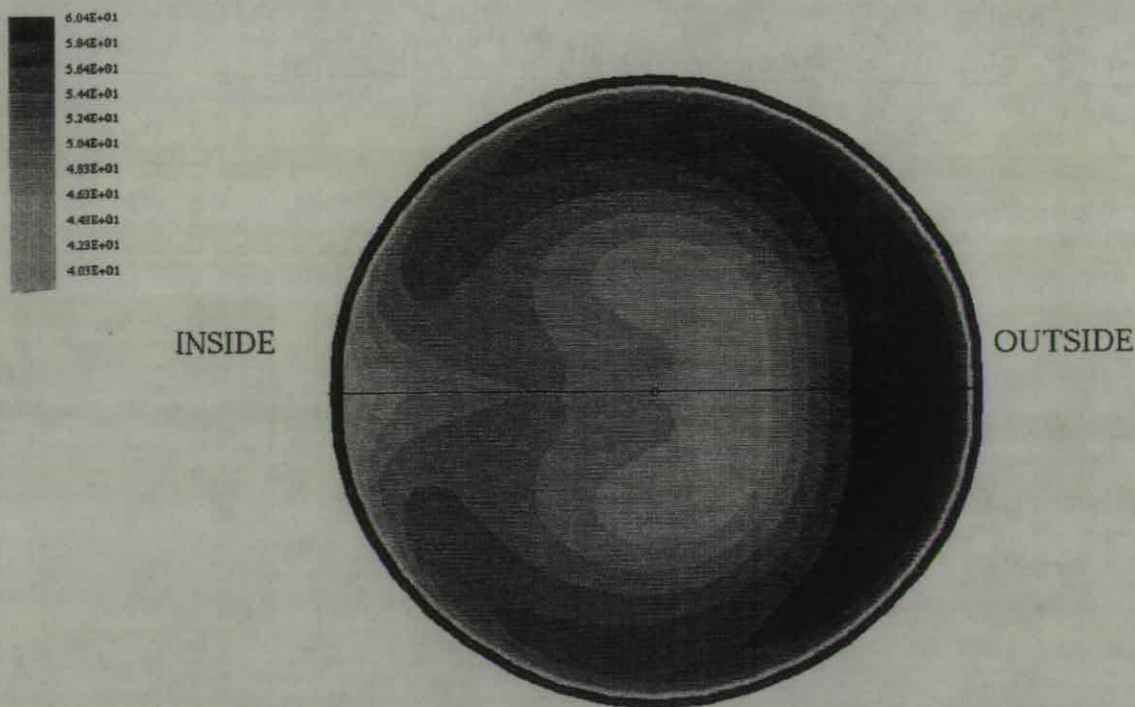
Velocity Magnitude (M/S)

L max = 6.113E+01 L min = 0.000E+00

Fluent 4.31

Fluent Inc.

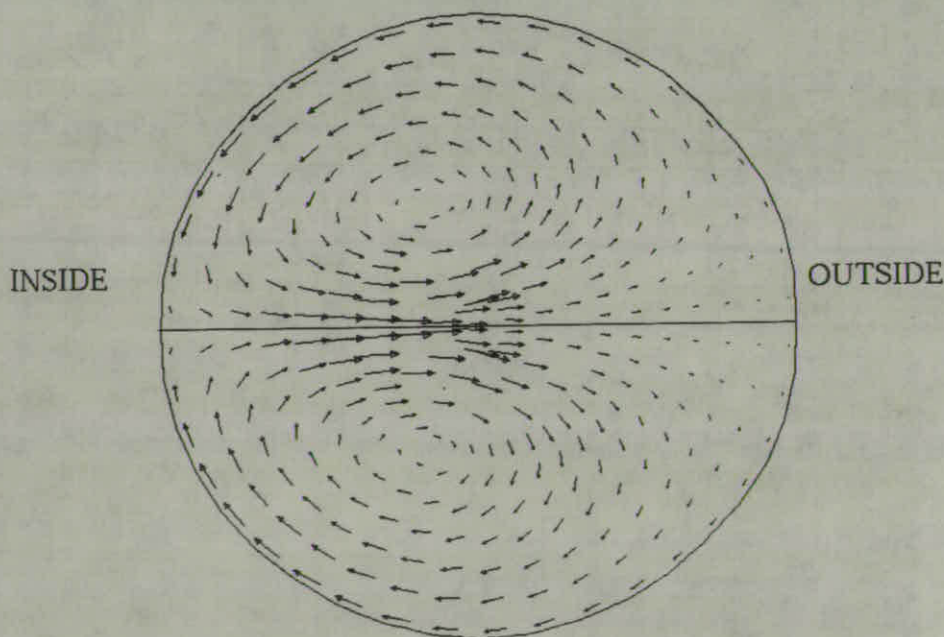
Fig. 5 Contours of Velocity Magnitude for Cross-sections Downstream of a Single Bend



NEL - Single 90 degree bend
 Velocity Magnitude (M/S)
 $L_{max} = 6.042E+01$ $L_{min} = 0.000E+00$

Fluent 4.31
 Fluent Inc.

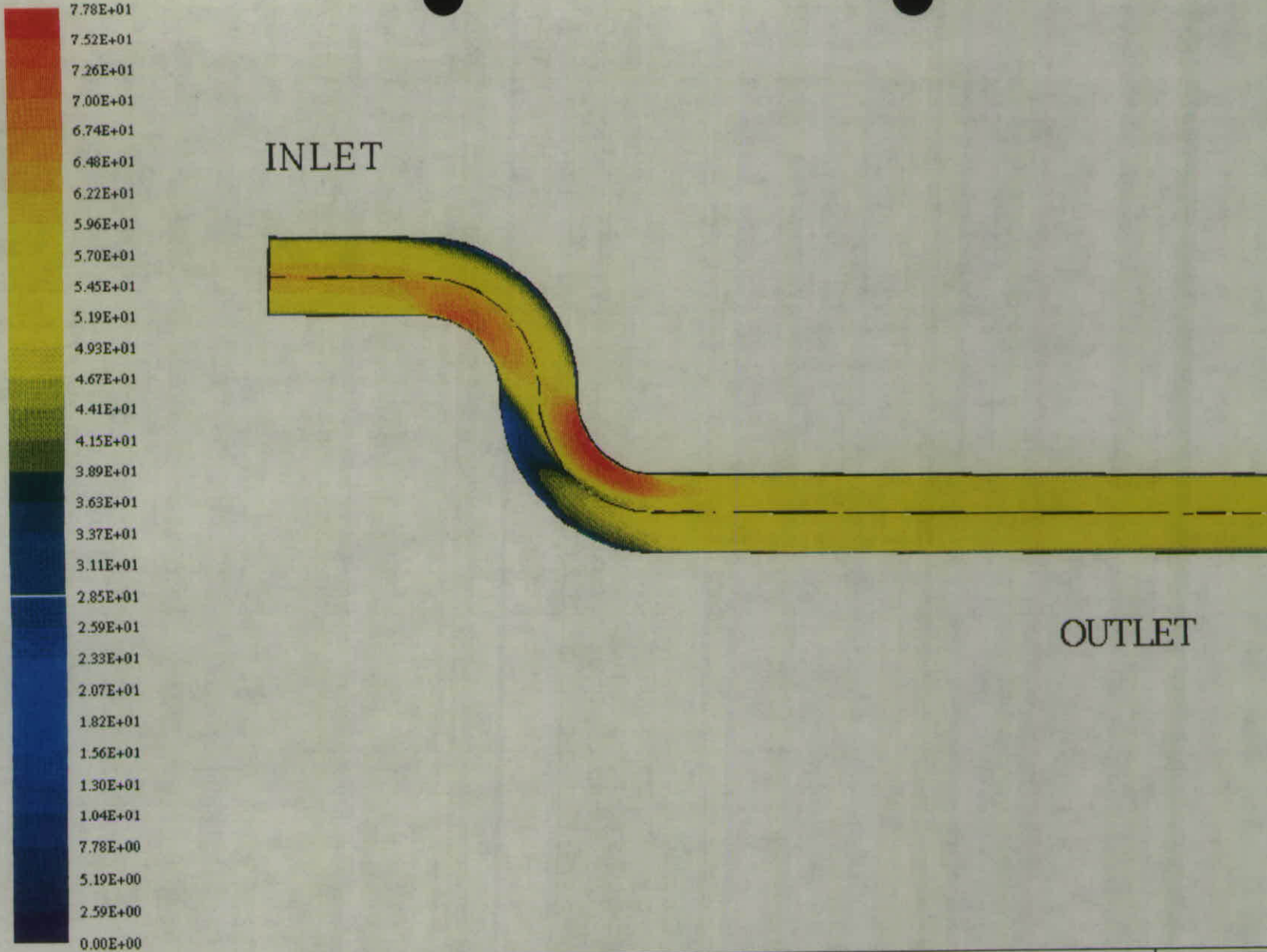
Fig. 6 Contours of Velocity Magnitude For a Cross-Section 4D Downstream of a Single Bend



NEL - Single 90 degree bend
 Velocity Vectors (M/S)

Sep 04 1995
 Fluent 4.31
 Fluent Inc.

Fig. 7 Velocity Vectors For a Cross-Section 4D Downstream of a Single Bend



NEL – S-bend with no separation

Velocity Magnitude (M/S)

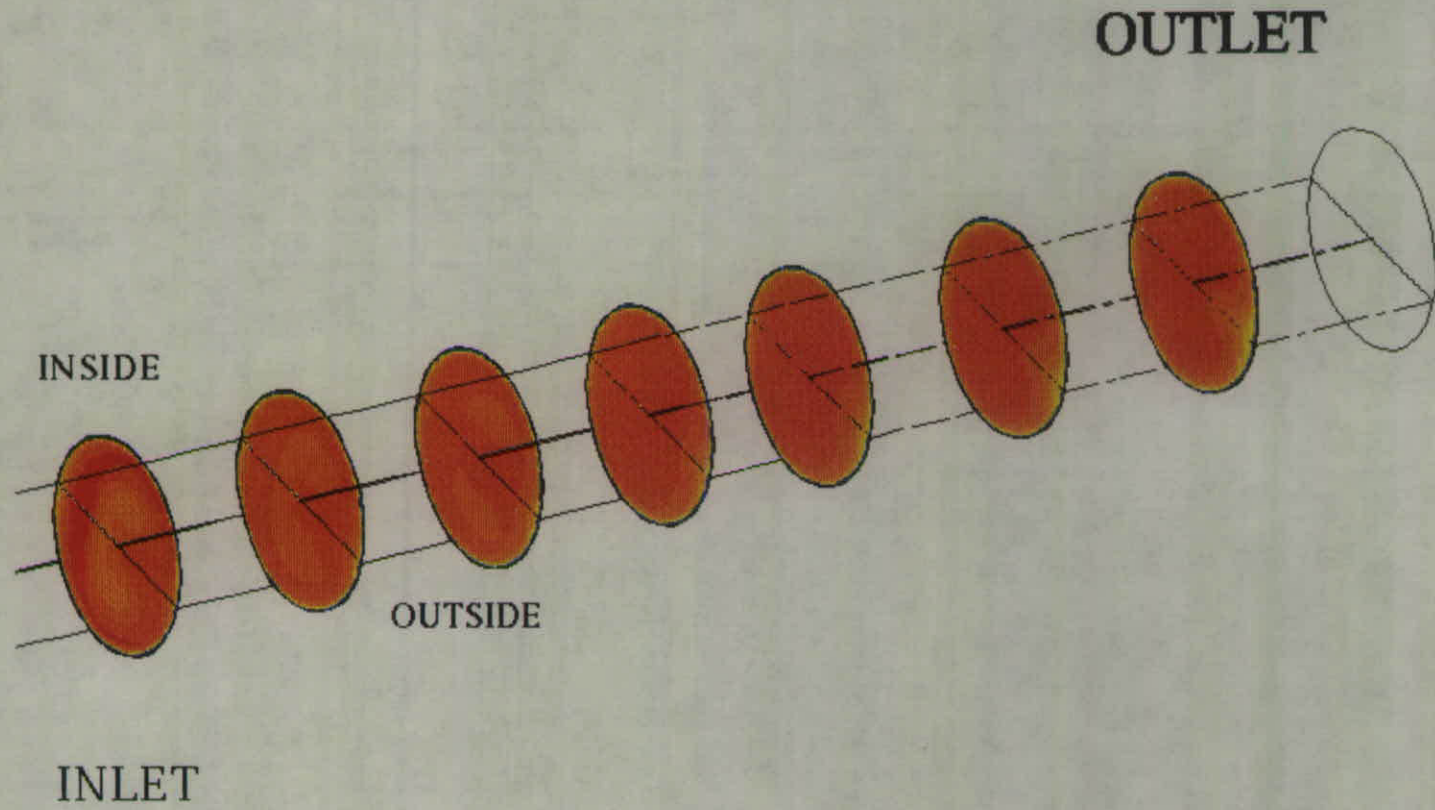
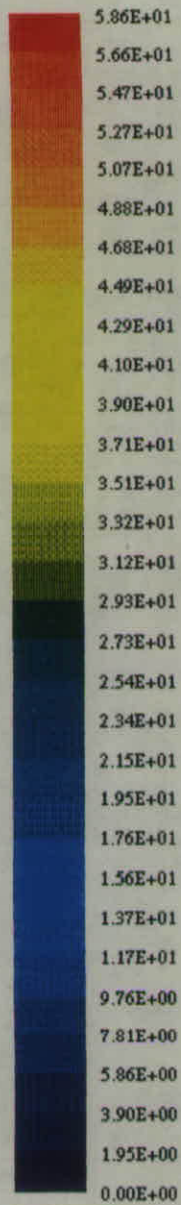
Lmax = 7.779E+01 Lmin = 0.000E+00



Fluent 4.31

Fluent Inc.

Fig. 8 Contours of Velocity Magnitude in the Plane of Symmetry for an S-Bend with no Separation



NEL – S-bend with no separation

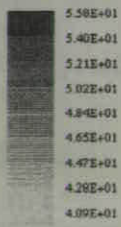
Velocity Magnitude (M/S)

Lmax = 5.856E+01 Lmin = 0.000E+00

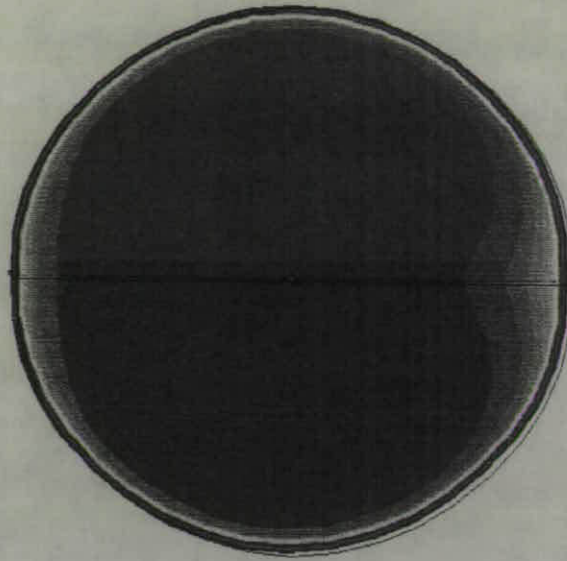
Fluent 4.31

Fluent Inc.

Fig. 9 Contours of Velocity Magnitude for Cross-sections Downstream of an S-Bend with no Separation



INSIDE



OUTSIDE

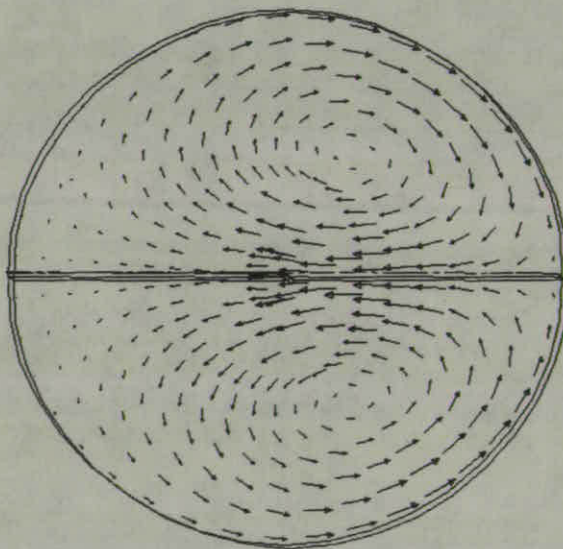


NEL - S-bend with no separation
Velocity Magnitude (M/S)
Lmax = 5.583E+01 Lmin = 0.000E+00

Fluent 4.31
Fluent Inc.

Fig. 10 Contours of Velocity Magnitude For a Cross-Section 4D Downstream of an S-Bend With No Separation

INSIDE

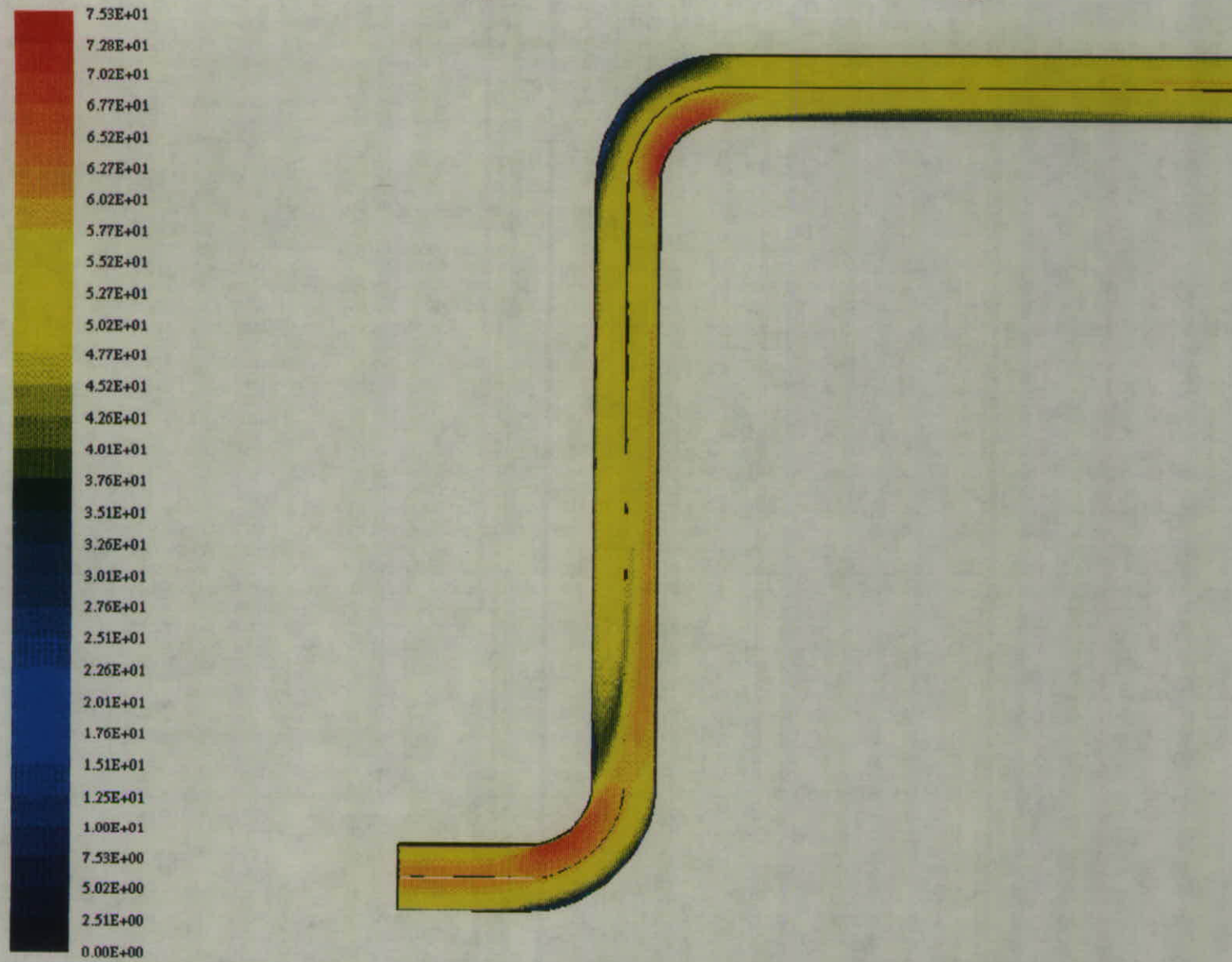


OUTSIDE

NEL - S-bend with no separation
Velocity Vectors (M/S)

Sep 05 1995
Fluent 4.31
Fluent Inc.

Fig. 11 Velocity Vectors For a Cross-Section 4D Downstream of an S-Bend With No Separation



NEL - S-bend with 9D separation

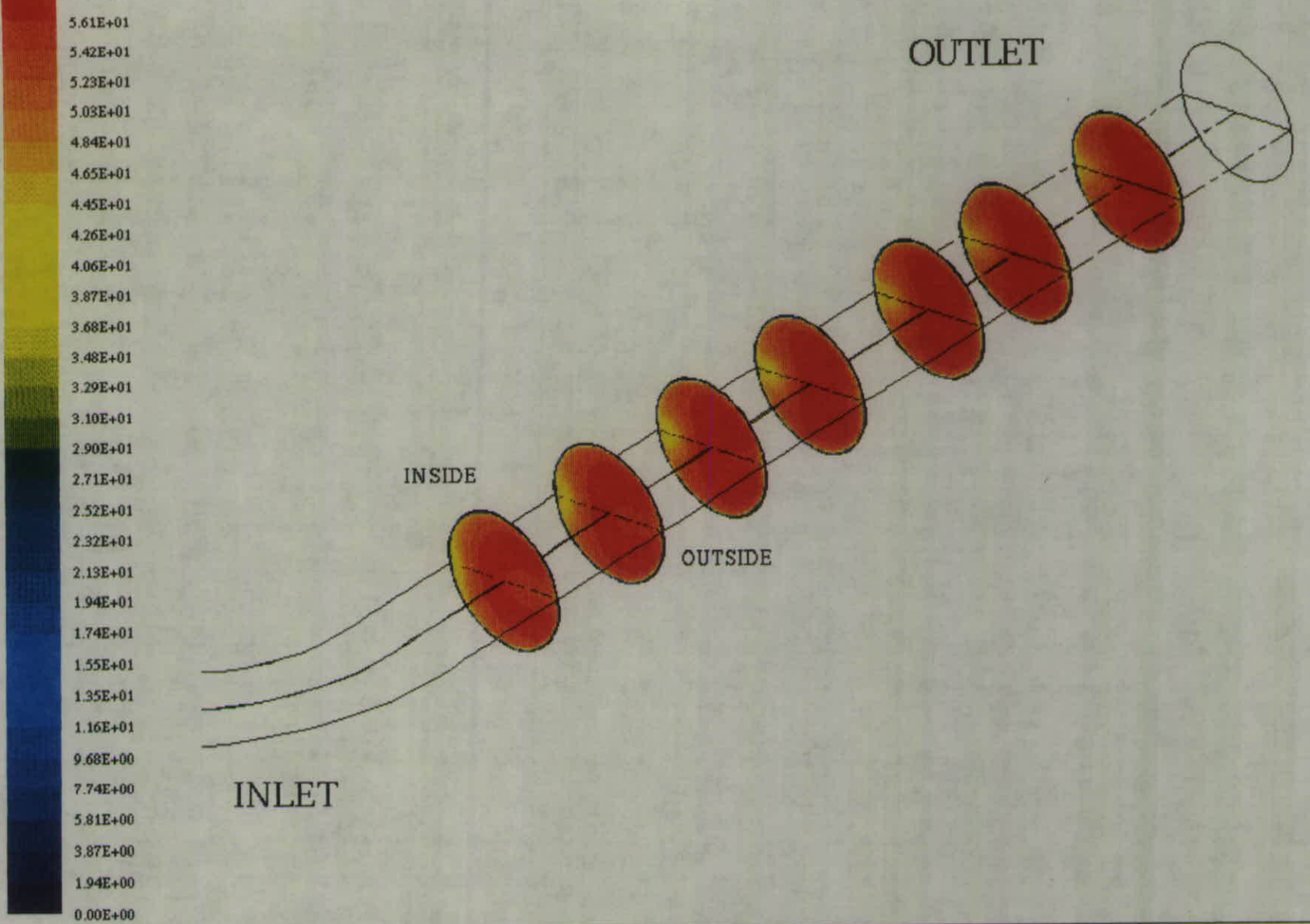
Velocity Magnitude (M/S)

Lmax = 7.526E+01 Lmin = 0.000E+00

Fluent 4.31

Fluent Inc.

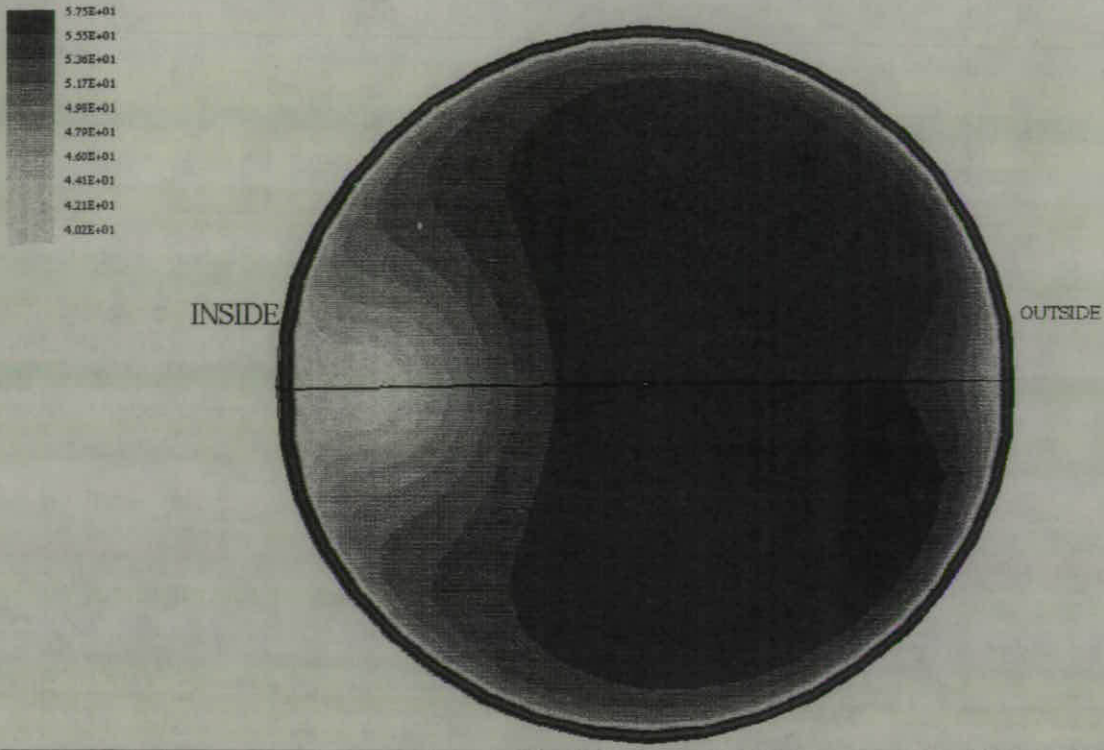
Fig. 12 Contours of Velocity Magnitude in the Plane of Symmetry for an S-Bend with 9D Separation



NEL - S-bend with 9D separation
Velocity Magnitude (M/S)
Lmax = 5.807E+01 Lmin = 0.000E+00

Fluent 4.31
Fluent Inc.

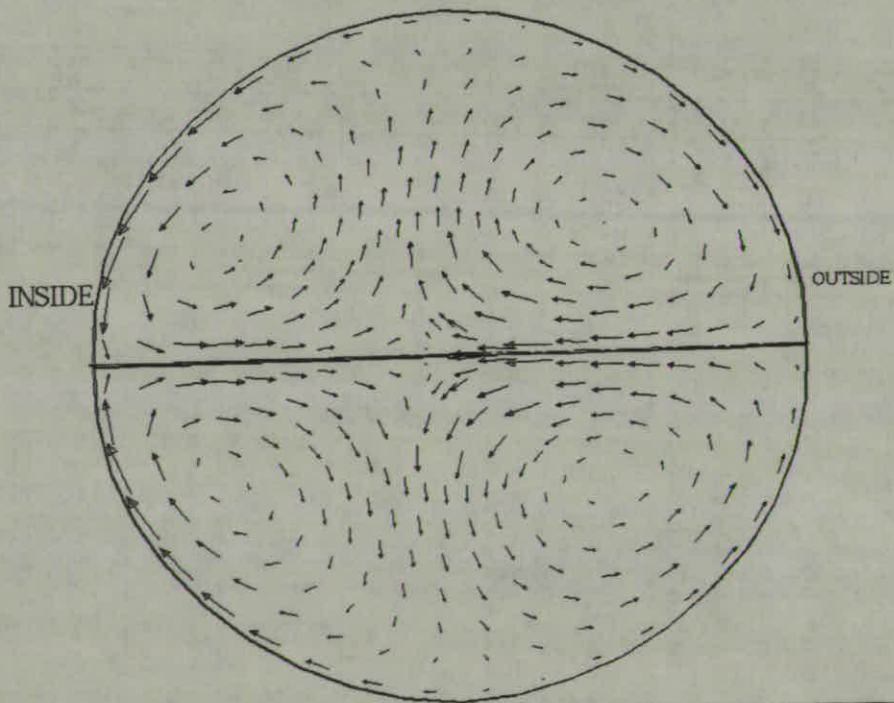
Fig. 13 Contours of Velocity Magnitude for Cross-sections Downstream of an S-Bend with 9D Separation



NEL - S-bend with 9D separation
 Velocity Magnitude (M/S)
 Lmax = 5.746E+01 Lmin = 0.000E+00

Fluent 4.31
 Fluent Inc.

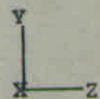
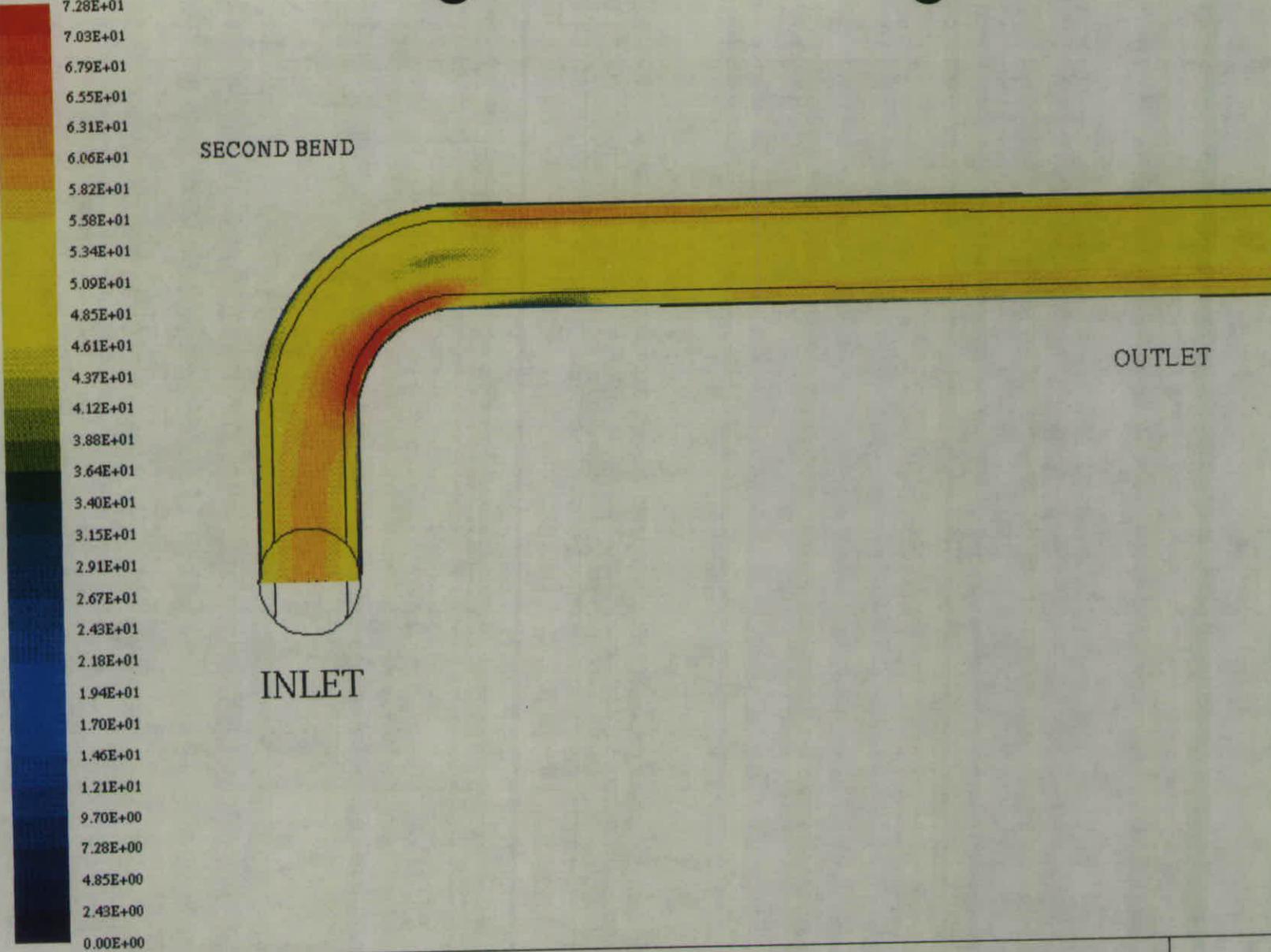
Fig. 14 Contours of Velocity Magnitude For a Cross-Section 4D Downstream of an S-Bend With 9D Separation



NEL - S-bend with 9D separation
 Velocity Vectors (M/S)

Sep 04 1995
 Fluent 4.31
 Fluent Inc.

Fig. 15 Velocity Vectors For a Cross-Section 4D Downstream of an S-Bend With 9D Separation



NEL – Twisted S-bend with no separation

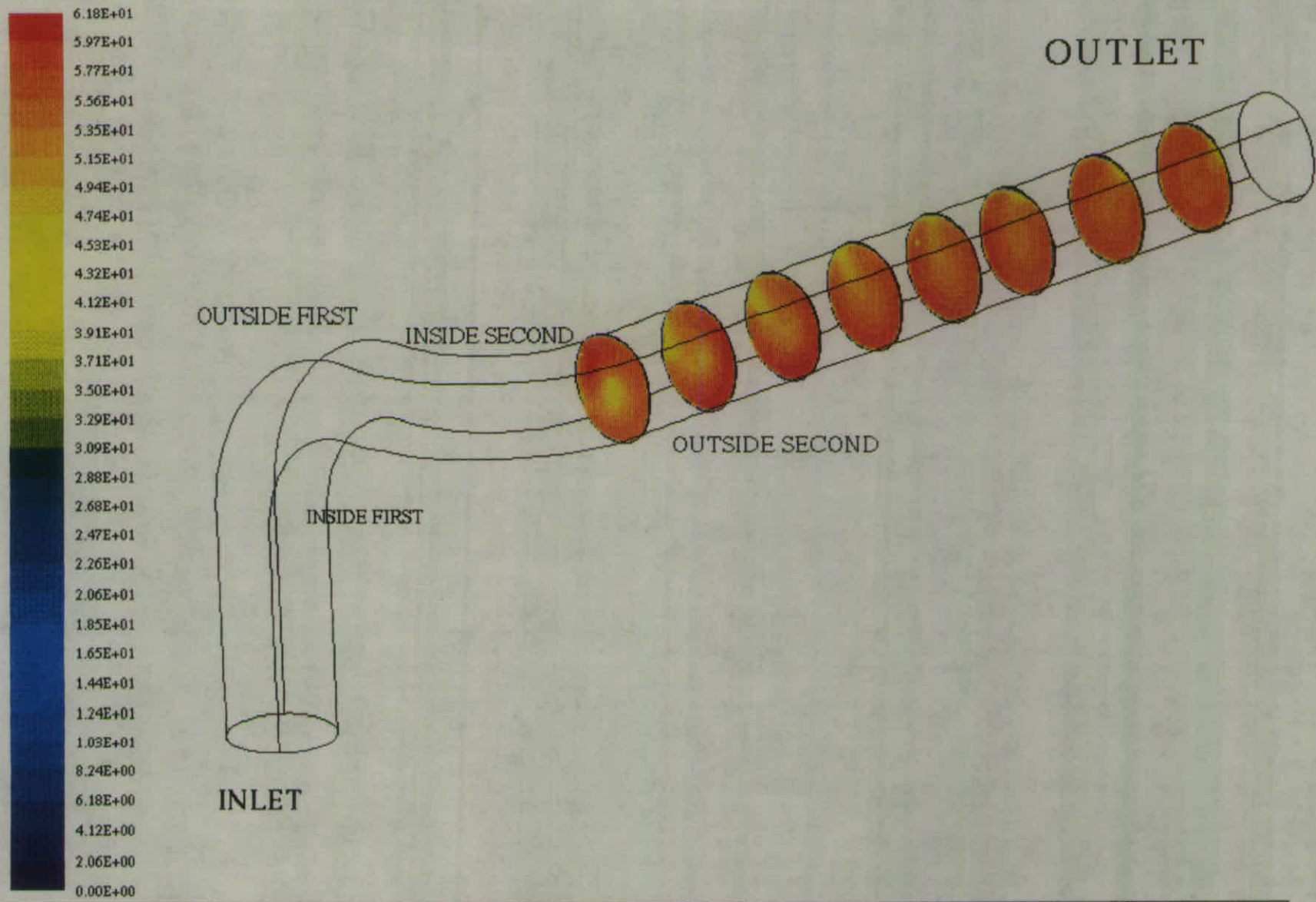
Velocity Magnitude (M/S)

$L_{max} = 7.275E+01$ $L_{min} = 0.000E+00$

Fluent 4.31

Fluent Inc.

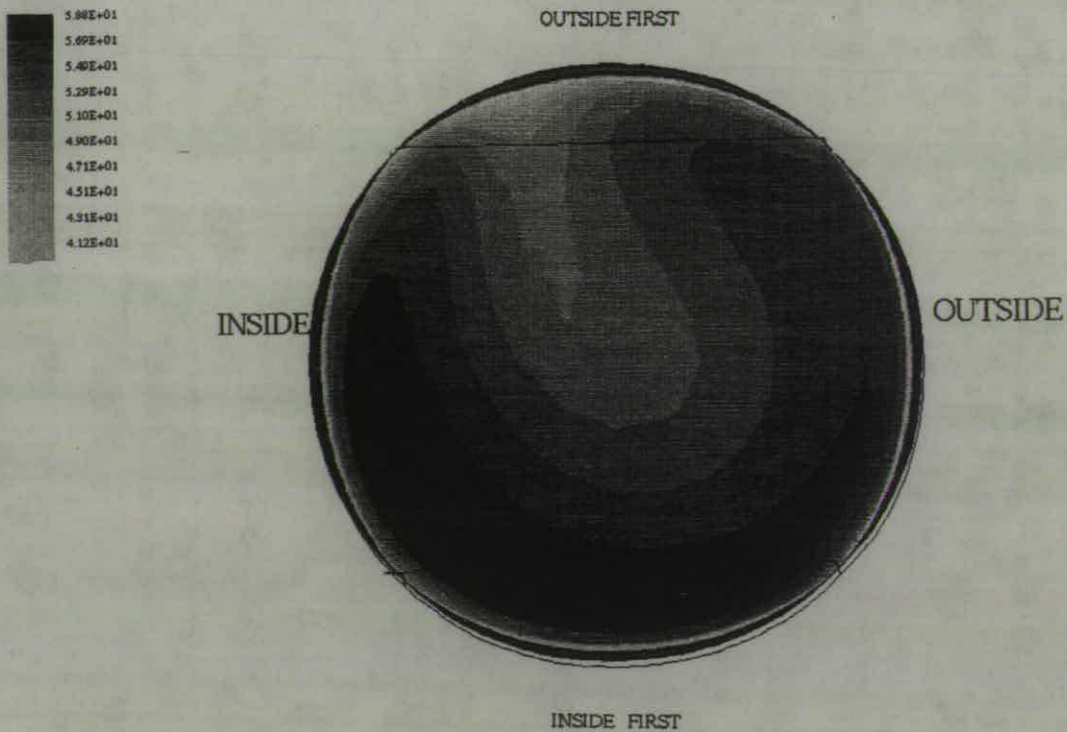
Fig. 16 Contours of Velocity Magnitude for a Twisted S-Bend in the Plane of Symmetry (With Respect to the Second Bend)



NEL - Twisted S-bend with no separation
Velocity Magnitude (M/S)
L max = 6.177E+01 L min = 0.000E+00

Fluent 4.31
Fluent Inc.

Fig. 17 Contours of Velocity Magnitude for Cross-sections Downstream of a Twisted S-Bend



NEL - Twisted S-bend with no separation

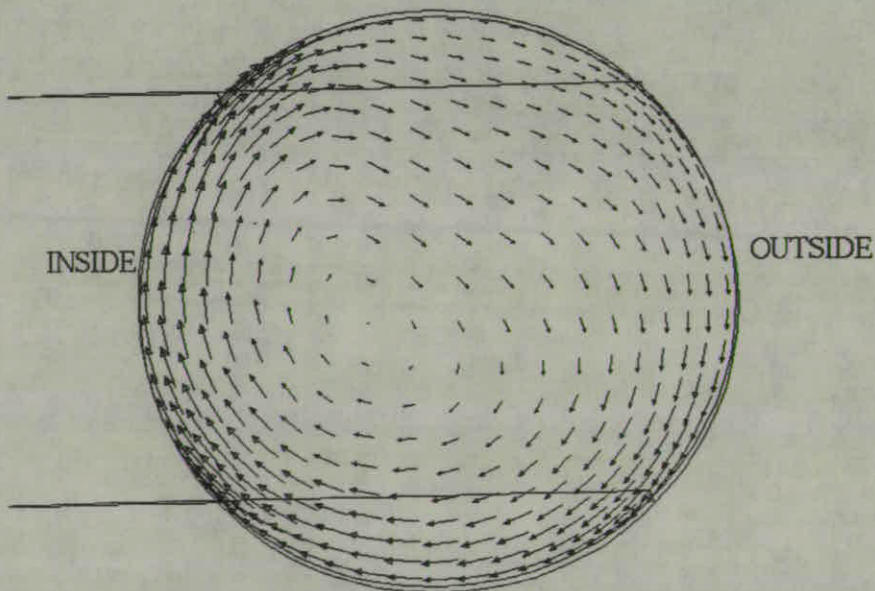
Velocity Magnitude (M/S)

Lmax = 5.881E+01 Lmin = 0.000E+00

Fluent 4.31

Fluent Inc.

Fig. 18 Contours of Velocity Magnitude For a Cross-Section 4D Downstream of a Twisted S-Bend



NEL - Twisted S-bend with no separation

Velocity Vectors (M/S)

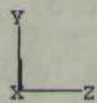
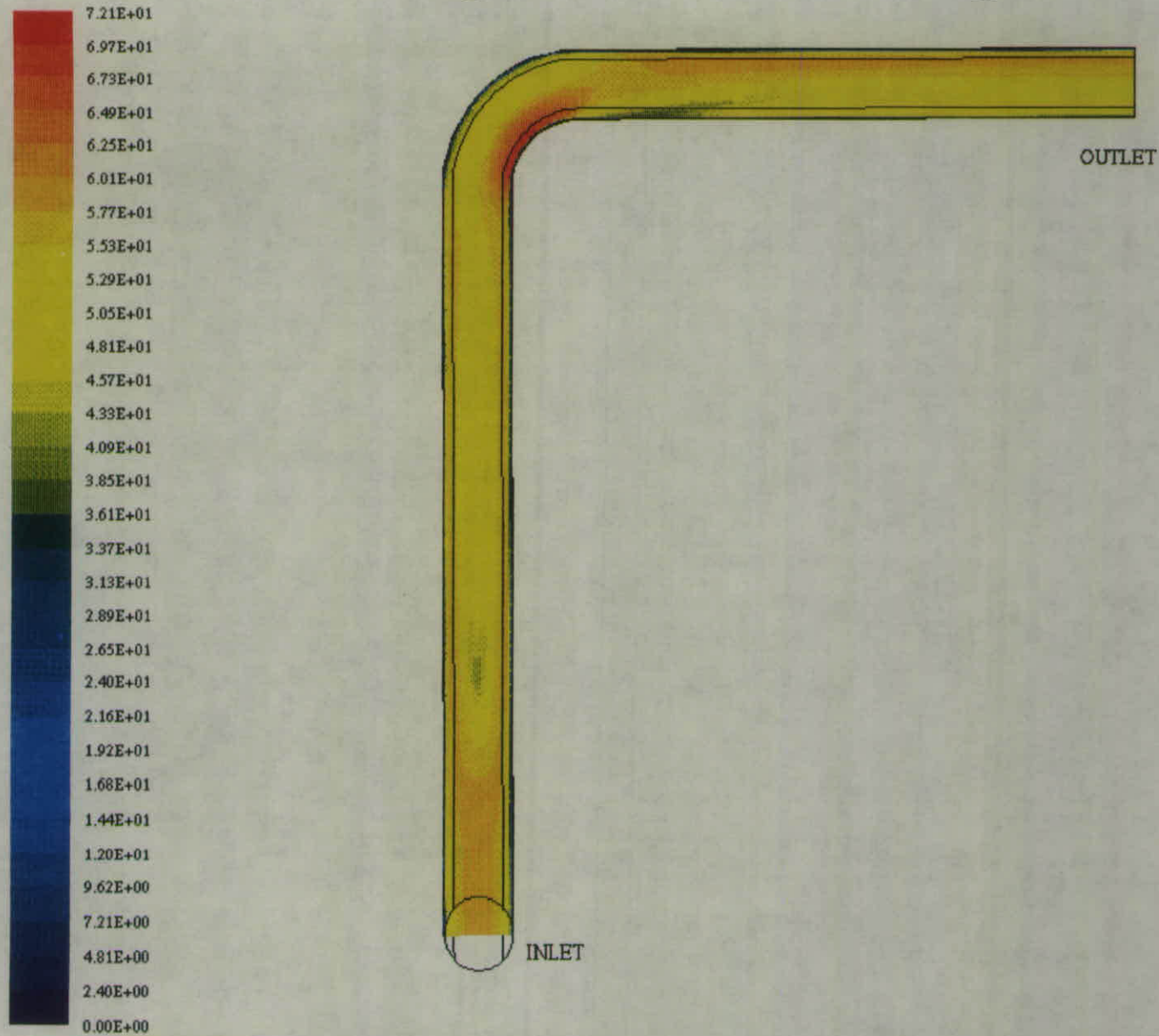
Lmax = 1.470E+01 Lmin = 4.320E-01

Sep 06 1995

Fluent 4.31

Fluent Inc.

Fig. 19 Velocity Vectors For a Cross-Section 4D Downstream of a Twisted S-Bend



NEL – Twisted S-bend with 9D separation

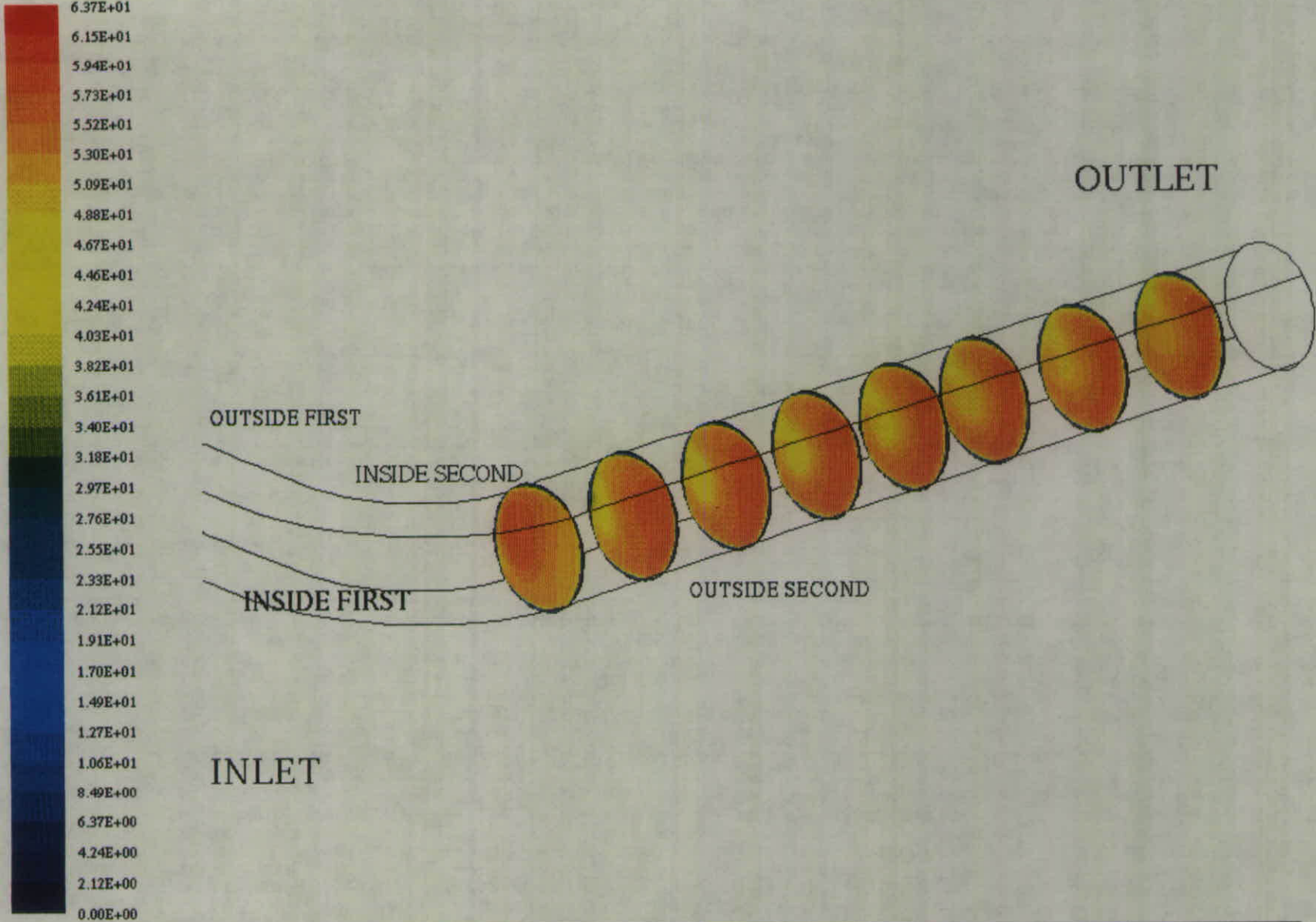
Velocity Magnitude (M/S)

Lmax = 7.215E+01 Lmin = 0.000E+00

Fluent 4.31

Fluent Inc.

Fig. 20 Contours of Velocity Magnitude for a Twisted S-Bend with 9D Separation in the Plane of Symmetry (With Respect to the Second Bend)



NEL – Twisted S-bend with 9D separation

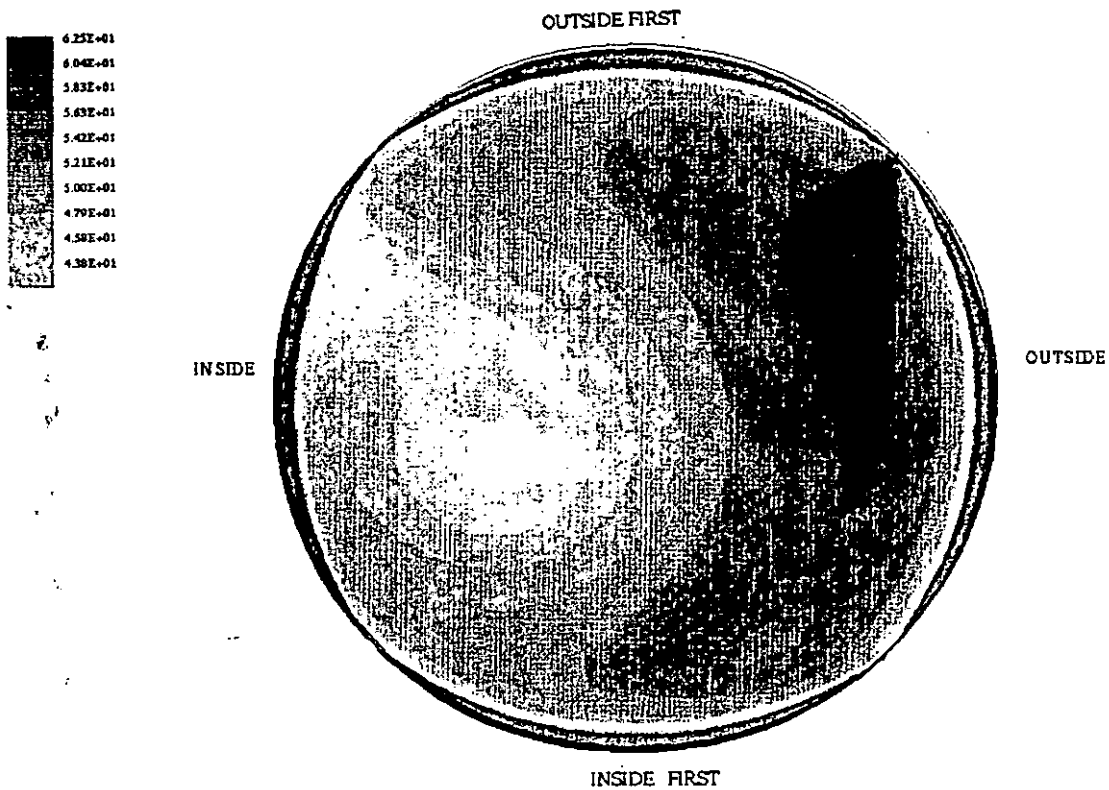
Velocity Magnitude (M/S)

Lmax = 6.366E+01 Lmin = 0.000E+00

Fluent 4.31

Fluent Inc.

Fig. 21 Contours of Velocity Magnitude for Cross-sections Downstream of a Twisted S-Bend with 9D Separation



NEL - Twisted S-bend with 9D separation

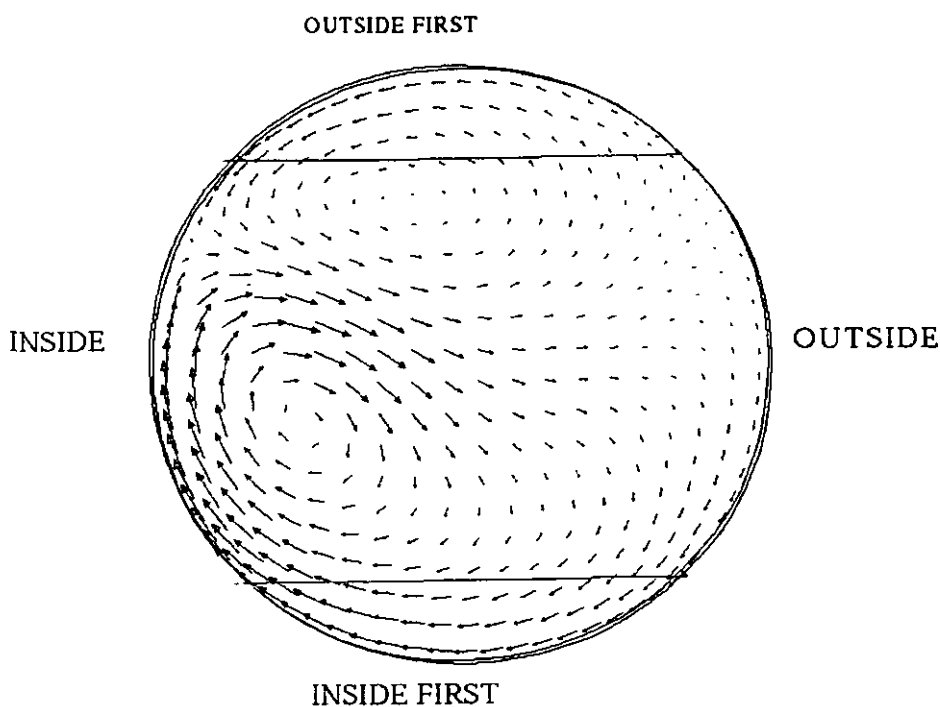
Velocity Magnitude (M/S)

Lmax - 6.252E+01 Lmin - 0.000E+00

Fluent 4.31

Fluent Inc.

Fig. 22 Contours of Velocity Magnitude For a Cross-Section 4D Downstream of a Twisted S-Bend With 9D Separation



NEL - Twisted S-bend with 9D separation

Velocity Vectors (M/S)

Lmax - 9.420E+00 Lmin - 5.965E-02

Sep 12 1996

Fluent 4.31

Fluent Inc.

Fig. 23 Velocity Vectors For a Cross-Section 4D Downstream of a Twisted S-Bend With 9D Separation

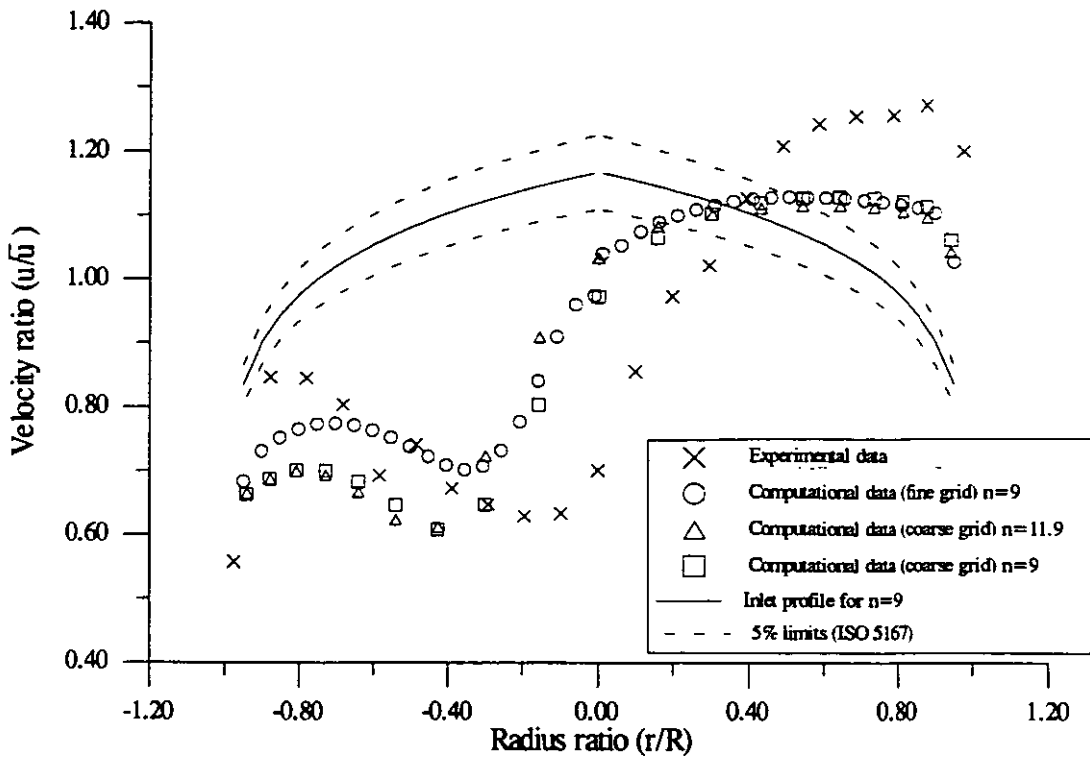


Fig. 24 Comparison of Experimental and Computational Axial Velocity Profiles 7/8D Downstream of a Single Bend on the Plane of Symmetry

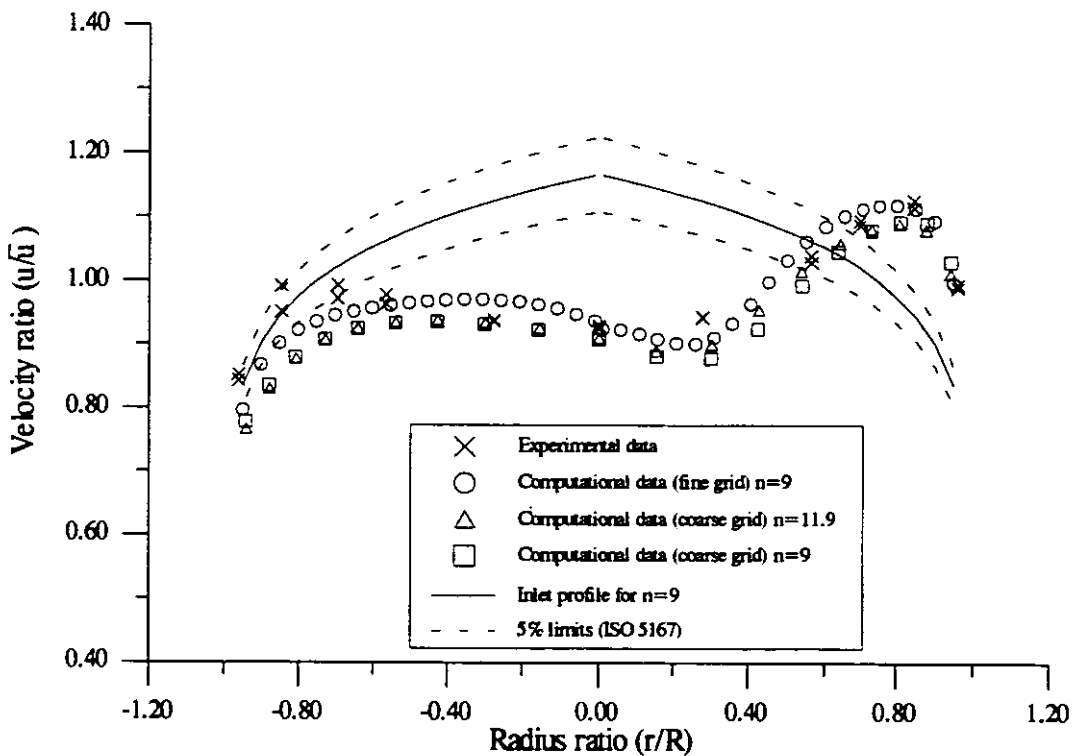


Fig. 25 Comparison of Experimental and Computational Axial Velocity Profiles 4D Downstream of a Single Bend on the Plane of Symmetry

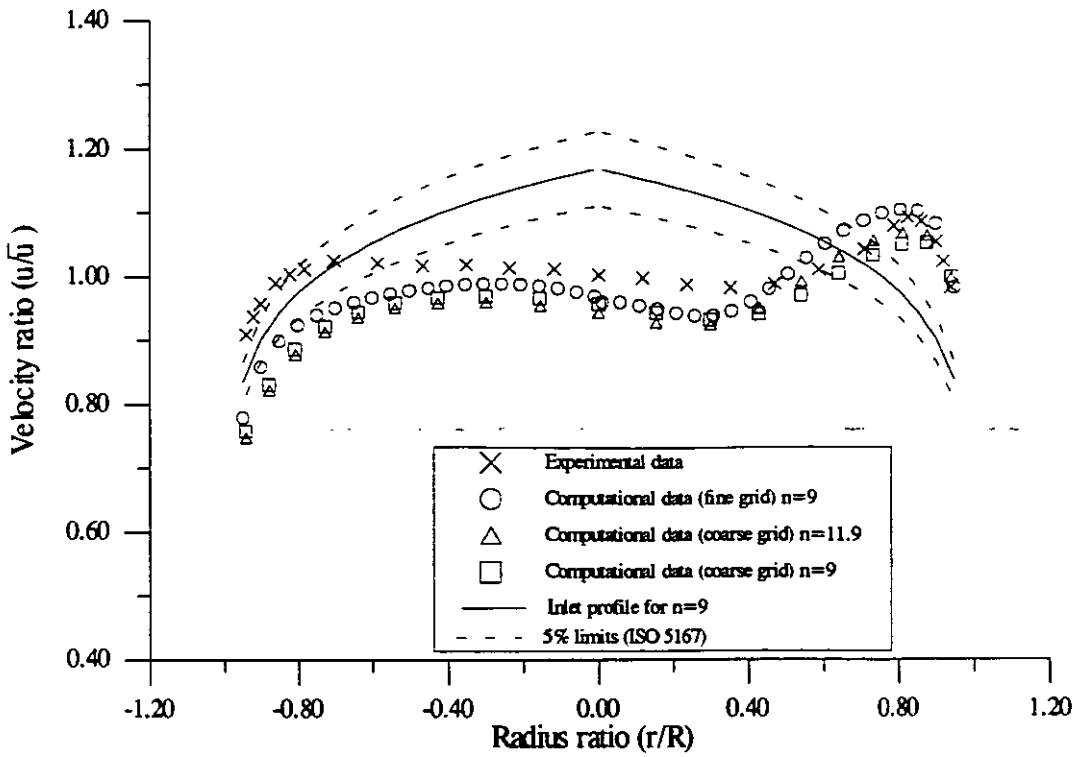


Fig. 26 Comparison of Experimental and Computational Axial Velocity Profiles 5D Downstream of a Single Bend on the Plane of Symmetry

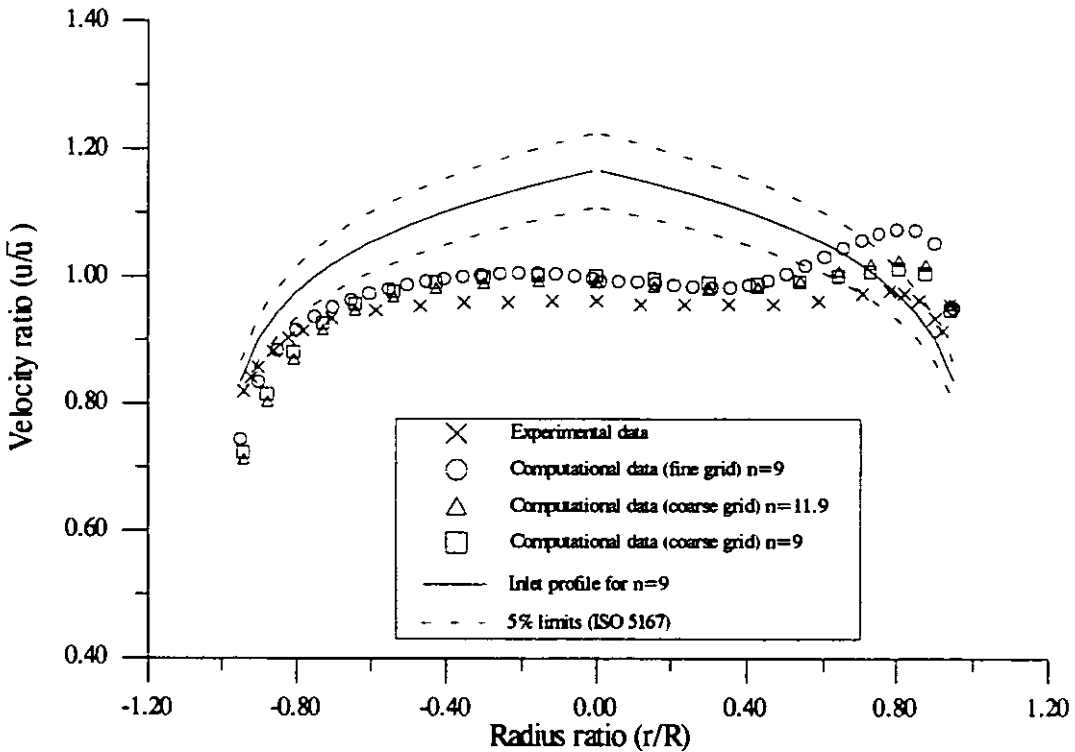


Fig. 27 Comparison of Experimental and Computational Axial Velocity Profiles 7D Downstream of a Single Bend on the Plane of Symmetry

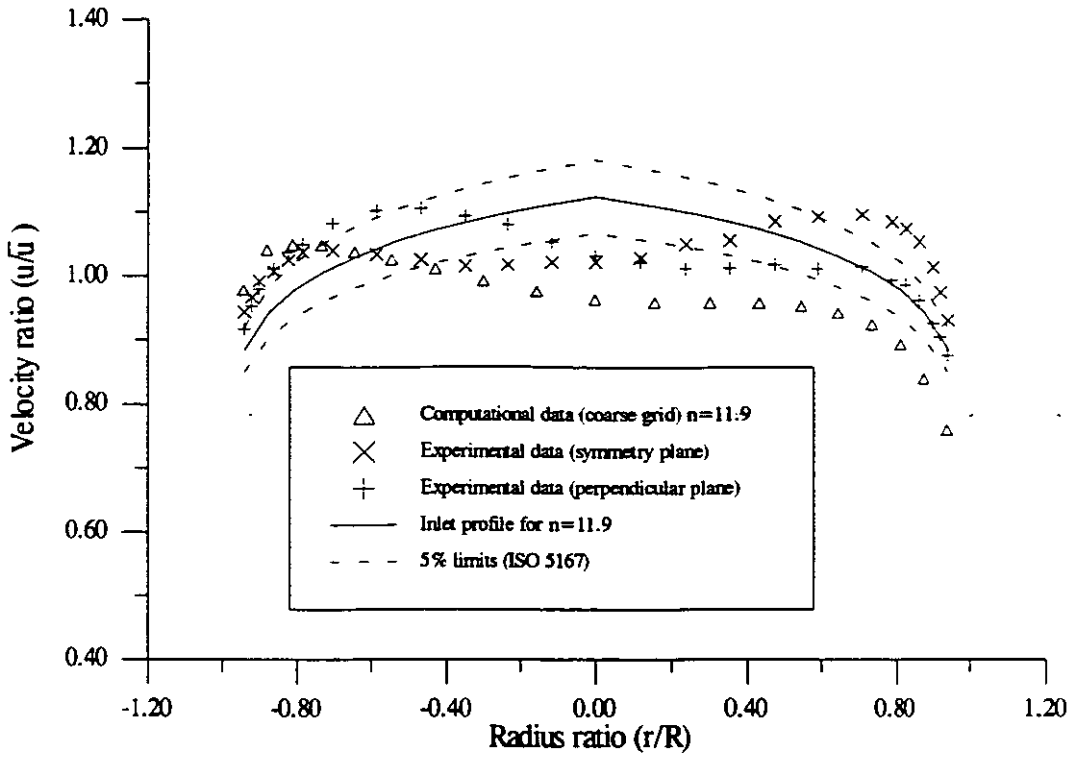


Fig. 28 Comparison of Experimental and Computational Axial Velocity Profiles 5D Downstream of a Twisted S-Bend on the Plane of Symmetry (With Respect to the Second Bend)

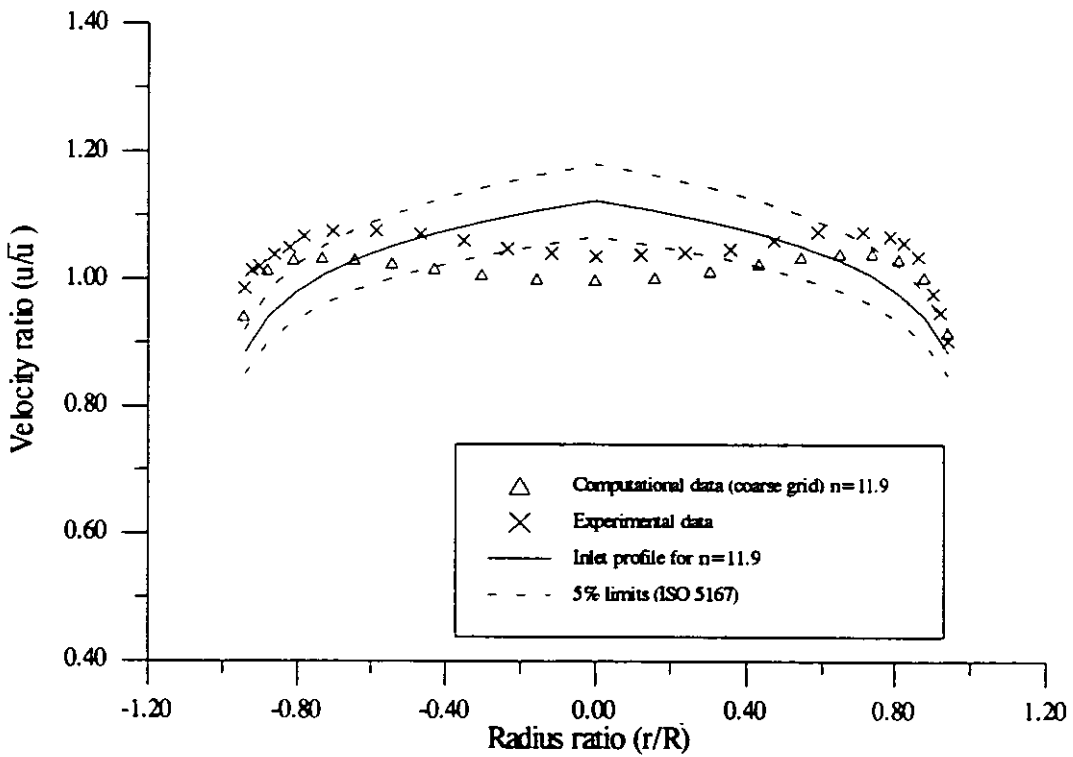


Fig. 29 Comparison of Experimental and Computational Axial Velocity Profiles 7D Downstream of a Twisted S-Bend on the Plane of Symmetry (With Respect to the Second Bend)